Cell Biology

A stable microtubule bundle formed through an orchestrated multistep process controls quiescence exit

Damien Laporte ✉, **Aurélie Massoni-Laporte, Charles Lefranc, Jim Dompierre, David Mauboules, Emmanuel. T. Nsamba, Anne Royou, Lihi Gal, Maya Schuldiner, Mohan L. Gupta Jr, Isabelle Sagot**

Univ. Bordeaux, CNRS, IBGC, UMR 5095, Bordeaux, France • Genetics, Development, and Cell Biology, Iowa State University, Ames, IA 50011, USA • Department of Molecular Genetics, Weizmann Institute of Science, Rehovot, Israel

Reviewed Preprint

Revised by authors after peer review.

About eLife's process

Reviewed preprint version 2
February 27, 2024 (this version)

Reviewed preprint version 1
September 1, 2023

Sent for peer review
June 30, 2023

Posted to preprint server
May 3, 2023

Abstract

Cells fine-tune microtubule assembly in both space and time, to give rise to distinct edifices with specific cellular functions. In proliferating cells, microtubules are highly dynamics, and proliferation cessation often leads to their stabilization. One of the most stable microtubule structures identified to date is the nuclear bundle assembled in quiescent yeast. In this report, we characterize the original multistep process driving the assembly of this structure. This AuroraB-dependent mechanism follows a precise temporality that relies on the sequential actions of kinesin-14, kinesins-5 and involves both microtubule-kinetochore and kinetochore-kinetochore interactions. Upon quiescence exit, the microtubule bundle is disassembled via a cooperative process involving kinesin-8 and its full disassembly is required prior to cells re-entry into proliferation. Overall, our study provides the first description, at the molecular scale, of the entire life cycle of a stable microtubule structure *in vivo*, and sheds light on its physiological function.

eLife assessment

This work presents **important** insights regarding the mechanism underlying the assembly, maintenance, and disassembly of a very stable microtubule-based structure, termed quiescent-cell nuclear microtubule (Q-nMT) bundle, which is formed in quiescent yeast cells to ensure cell survival and viability. This insight will help to elucidate how very stable microtubules can exist alongside very dynamic microtubules, which is still poorly understood. While the experimental support is overall **solid**, additional analyses using state-of-the-art methodology would further strengthen some of the claims.

Introduction

Microtubules (MTs) are hollow cylindrical polymers assembled by the non-covalent interaction of α- and β-tubulin heterodimers. MTs are generally nucleated at MT organizing centers (MTOC) by a γ-tubulin complex (γ-TuC) which acts as a template and stabilizes the so-called MT "minus-end" (Liu et al., 2021; Roostalu and Surrey, 2017; Sanchez and Feldman, 2017; Thawani and Petry, 2021). At the opposite end, the "plus-end" (+end), MTs elongate by the addition of GTP tubulin. The β-tubulin bound GTP is hydrolyzed, and stable but transient, GDP + Pi intermediates are generated in the region immediately behind the growing +end. Subsequent Pi release favors MT depolymerization which can be rescued by *de novo* GTP-tubulin addition (Cleary and Hancock, 2021; Gudimchuk and McIntosh, 2021). Thus, MTs alternate between periods of growth and shrinkage, a behavior termed dynamic instability (Mitchison and Kirschner, 1984). *In vivo*, a profusion of MT-associated proteins (MAPs) regulate MT length and dynamics (Bodakuntla et al., 2019; Goodson and Jonasson, 2018). In addition, MTs are often assembled from multiple tubulin variants or isotypes, and are modified by a cohort of post-translational modifications that modulate MT dynamics directly or by influencing the recruitment of MAPs (Janke and Magiera, 2020; Roll-Mecak, 2020). Other MAPs organize MTs into highly-ordered assemblies either by cross-linking MTs or by connecting them with cellular structures such as membranes, chromosomes, or actin cytoskeleton components (Bodakuntla et al., 2019; Meiring et al., 2020). Cells fine-tune these mechanisms in both space and time to give rise to distinct MT edifices with specific functions.

In proliferating cells, MT dynamics are crucial for their functions. It allows exploration of the cell volume in search of structures to "capture", such as centromeres during mitosis, or to exert pushing or pulling forces required for various cellular processes such as cell migration or morphogenesis (Heald and Khodjakov, 2015; Kirschner and Mitchison, 1986). The MT cytoskeleton can undergo extensive rearrangements and assemble more stable MT structures, especially when cells change fate (Meiring et al., 2020; Röper, 2020). For example, in terminally differentiated cells, such as epithelial cells, cardiomyocytes or neurons, stable MT networks make up the majority, and ensure critical cellular functions such as cell shape maintenance or long-distance intracellular transport (Baas et al., 2016; Muroyama and Lechler, 2017). Defects in MT stabilization are at the origin of many human pathologies, including neurodegenerative diseases and ciliopathies (Anvarian et al., 2019; Wheway et al., 2018). Effectors responsible for MT stabilization have been actively searched for since the 1980's. In mammals, the involvement of specific MAPs such as Tau, MAP2, MAP6 and PRC1, or tubulin post-translational modifications has been extensively studied. While their contributions to MT stabilization are central and undisputed, their sole actions do not fully explain the observed levels of MT stability in many types of non-dividing cells (Hahn et al., 2019).

For years, yeast species have been instrumental in unraveling mechanisms that regulate MT dynamics in eukaryotes. While proliferating yeast cells exhibit a dynamic MT network (Winey and Bloom, 2012), proliferation cessation goes with the formation of dramatically stable MT structures in both *S. cerevisiae* and *S. pombe* (Laporte and Sagot, 2014; Laporte et al., 2013, 2015). Upon quiescence establishment, *S. cerevisiae* cells assemble a bundle composed of stable parallel MTs, hereafter referred to as the Q-nMT bundle, for Quiescent-cell nuclear Microtubule bundle. This structure originates from the nuclear side of the spindle pole body (SPB), the yeast equivalent of the centrosome. It spans the entire nucleus and relocalizes kinetochores and centromeres, which remain attached to MT +ends (Laporte and Sagot, 2014; Laporte et al., 2013). Because the MTs embedded in the Q-nMT bundle are not all of the same length, the structure has a typical arrow shape. When cells exit quiescence, the Q-nMT bundle depolymerizes and, by pulling the attached centromeres back to the SPB, allows the recovery of the typical Rabl-like configuration of chromosomes found in G1 yeast cells (Jin et al., 1998). The molecular mechanisms underlying the formation of this peculiar stable MT structure and its physiological

function(s) are not understood. However, cells defective in Q-nMT bundle formation have a compromised survival in quiescence and a drastically reduced fitness upon cell cycle re-entry (Laporte and Sagot, 2014; Laporte et al., 2013, 2015).

Here, we show that Q-nMT bundle formation is a multistep process that follows a precise temporal sequence. The first step relies on AuroraB/Ipl1 activity and requires the kinesin-14 Kar3, its regulator Cik1, and the EB1 homolog Bim1. It leads to the formation of a short (≈ 1 µm) and stable bundle that resembles a half mitotic spindle. Importantly, in this first step, MT polymerization and stabilization are coupled. In a second step, additional MTs polymerize from the SPB, elongate, and are zipped to pre-existing MTs in a Cin8/kinesin-5 dependent manner. Complete stabilization of the Q-nMT bundle is achieved in a third and final step that requires the kinesin-5 Kip1. Our observations further indicate that Q-nMT bundle assembly requires both MT-kinetochore attachment and inter-kinetochore interactions. Finally, we show that, upon exit from quiescence, the Q-nMT bundle disassembles from its +ends, each MT depolymerizing in coordination with its neighbors, via the action of the depolymerase Kip3, a member of the kinesin-8 family. Importantly we show that the complete disassembly of the Q-nMT bundle is required for cells to re-enter the proliferation cycle. Overall, this study describes the entire life cycle of a MT structure, from the molecular mechanisms involved in its formation and stabilization to its disassembly and further suggests that this atypical quiescent specific structure acts as a regulator, or “control point”, for cell cycle resumption upon exit from quiescence.

Results

The Q-nMT bundle formation is a three-step process

We have previously shown that the Q-nMT bundle observed in quiescent cells is a stable nuclear structure (Laporte et al., 2013). To investigate whether the stabilization of the Q-nMT bundle was concomitant with its assembly or whether it assembled first as a dynamic structure, and then gets stabilized, we quantified the Q-nMT bundle length (**Fig. 1A**) and thickness (**Fig. 1B**) upon quiescence establishment following carbon source exhaustion. We found that the Q-nMT bundle assembly process could be divided into 3 sequential phases. In an initial phase (phase I), MTs elongated from the SPB to reach ≈0.8 µm. The number of these MTs, referred to as phase I-MTs, was approximately the same as in a mitotic spindle (see inset of **Fig. 1B** and Sup. Fig. 1A). Importantly, phase I-MTs were resistant to nocodazole (Noc), a MT poison that causes dynamic MT depolymerization, indicating that phase I-MT stabilization was concomitant with their polymerization (**Fig. 1A-B**). In a second phase, beginning ≈10h after glucose exhaustion, additional MTs emerged from the SPB (phase II-MTs) and elongated along phase-I MTs, nearly doubling the thickness of the phase I MT bundle (**Fig. 1B** and Sup. Fig. 1A). At this stage, the tip of the newly elongated MTs were unstable (**Fig. 1A-B**). Complete stabilization of the Q-nMT bundle was achieved ≈48h after glucose exhaustion (phase III). Indeed, after this step, a Noc treatment did not affect either the length or the thickness of the Q-nMT bundle (**Fig. 1A-B** and Sup. Fig. 1B). Plotting Q-nMT bundle width as a function of length for each individual cell, before and after Noc treatment further revealed the 3 successive phases of the Q-nMT bundle formation (**Fig. 1C**). Of note, Q-nMT bundles were also observed both in diploid cells upon glucose exhaustion (Sup. Fig. 1C) and in haploid cells transferred to water (Sup. Fig. 1D).

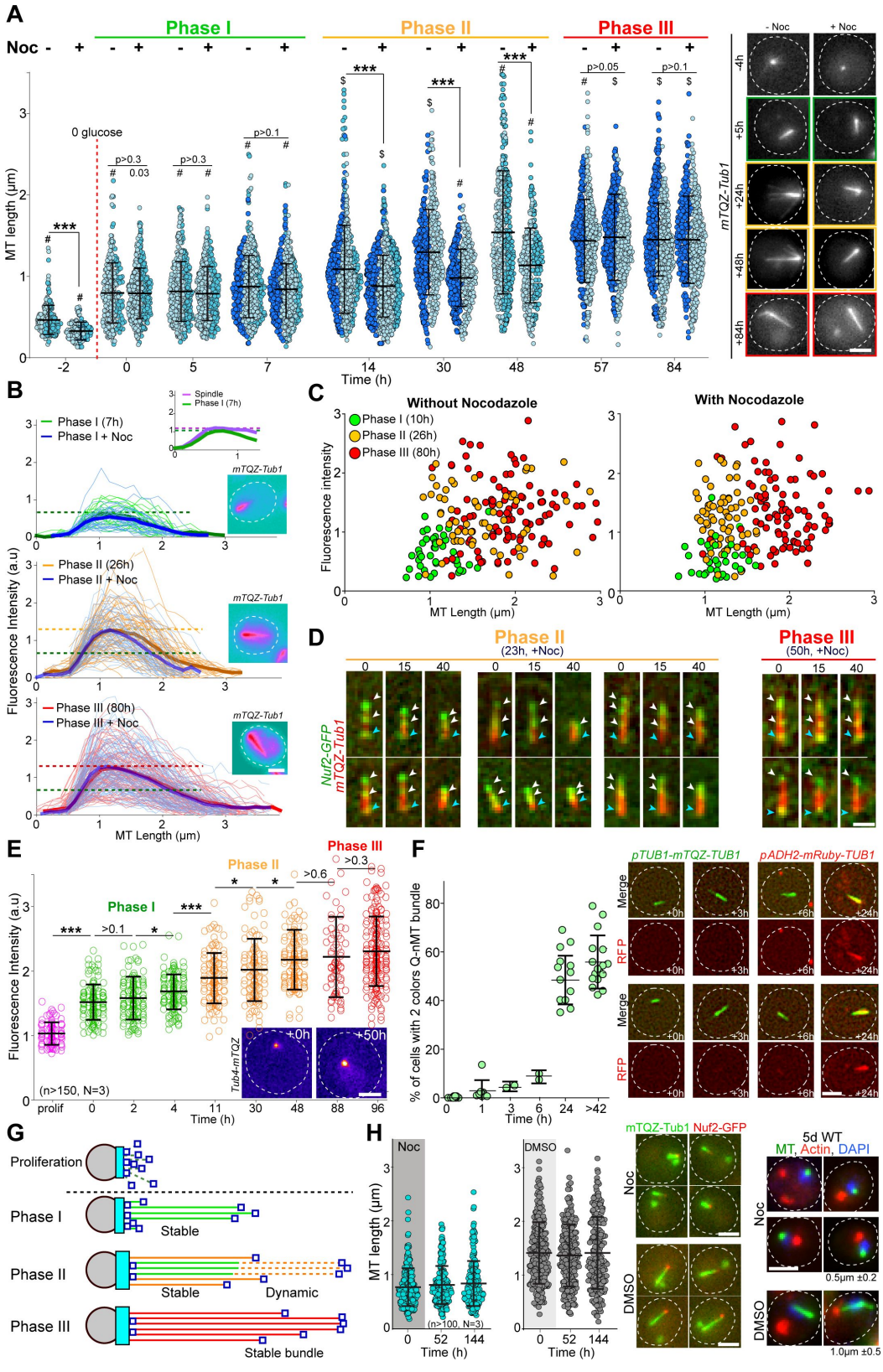
A
Phase I
Phase II
Phase III
Noc - + - + - + - + - + - + - + - + - + - +
0 glucose
MT length (µm)
Time (h)
-2 0 5 7 14 30 48 57 84
p>0.3
0.03
p>0.1
p>0.05
***
- Noc
+ Noc
mTQZ-Tub1
-4h
+5h
+24h
+48h
+84h
B
Phase I (7h)
Phase I + Noc
Phase II (26h)
Phase II + Noc
Phase III (80h)
Phase III + Noc
Spindle
Phase I (7h)
mTQZ-Tub1
Fluorescence Intensity (a.u)
MT Length (µm)
C
Without Nocodazole
With Nocodazole
Phase I (10h)
Phase II (26h)
Phase III (80h)
Fluorescence intensity
MT Length (µm)
D
Phase II
(23h, +Noc)
Phase III
(50h, +Noc)
Nuf2-GFP
mTQZ-Tub1
0 15 40
E
Phase I
Phase II
Phase III
>0.1
>0.3
>0.6
Fluorescence Intensity (a.u)
(n>150, N=3)
prolif 0 2 4 11 30 48 88 96
Time (h)
Tub4-mTQZ
+0h
+50h
F
pTUB1-mTQZ-TUB1
pADH2-mRuby-TUB1
Merge
RFP
+0h +3h +6h +24h
% of cells with 2 colors Q-nMT bundle
0 1 3 6 24 >42
Time (h)
G
Proliferation
Phase I
Stable
Phase II
Stable
Dynamic
Phase III
Stable bundle
H
Noc
DMSO
MT length (µm)
(n>100, N=3)
0 52 144
Time (h)
mTQZ-Tub1 Nuf2-GFP
5d WT
MT, Actin, DAPI
0.5µm ±0.2
1.0µm ±0.5

Figure 1

The formation of the Q-nMT bundle is a three-step process

(A) Nuclear MT length in WT cells expressing mTQZ-Tub1, before (**-**) or after (**+**) a 15 min Noc treatment (30 µg/ml) upon entry into quiescence. Each circle corresponds to the length of an individual MT structure. The results for 3 independent experiments are shown (pale blue, cyan and dark blue, n > 160 for each point in each experiment). The mean and SD are shown. Student test or ANOVA (sample >2) were used to compare inter-replicates. #: p-value > 0.05, $: p-value < 0.05. A student test (t-test with two independent samples) was used to compare the results obtained with or without Noc, the indicated p-values being the highest measured among experiments. ***: p-value < 1.10^{-5}. Images of representative cells are shown. Bar is 2 µm.

(B) MT fluorescence intensity as a proxy of MT structure width in WT cells expressing mTQZ-Tub1. Mean intensity measurement for half pre-anaphase mitotic spindles (purple), phase I (green), phase II (orange) or phase III (red) Q-nMT bundle. A line scan along the MT structure for an individual cell is shown as thin line, the mean as a bold line (n > 60 / phase), all the lines being aligned at 0,5 µm before the fluorescence intensity increase onset on the SPB side. The blue lines are results obtained after a 15 min Noc treatment (30 µg/ml). In each graph, horizontal dashed line indicates the mean intensity. Images in pseudo-colors of a representative cell for each phase are shown. Bar is 2 µm.

(C) MT bundle length as a function of MT bundle width for individual cells in each phase before and after a 15 min Noc treatment (30 µg/ml) in WT cells expressing mTQZ-Tub1. Each circle represents an individual MT structure.

(D) WT cells expressing mTQZ-Tub1 (red) and Nuf2-GFP (green) in phase II (23 h) or phase III (50 h) were deposited on an agarose pad containing 30 µg/ml Noc and imaged. Blue arrowheads: SPB; white arrowheads: Nuf2-GFP clusters. Time is in min after deposition on the pad. Bar is 1 µm.

(E) Tub4-mTQZ fluorescence intensity measured at the SPB upon entry into quiescence. Each circle represents an individual cell. The mean and SD are shown; t-tests were used to compare independent samples (N = 3, n > 150), *: 0.05 > p-value > 1.10^{-3}, ***: p-value < 1.10^{-5}. Images in pseudo-colors of representative cells are shown. Bar is 2 µm.

(F) WT cells expressing mTQZ-Tub1 under the *TUB1* promoter and mRuby-Tub1 under the *ADH2* promoter. The percentage of cells harboring both mTQZ and mRuby fluorescence along the Q-nMT bundle is shown; each circle being the percentage for an independent experiment, with n > 200 counted for each experiment. The mean and SD are shown. Images of representative cells at the indicated time after glucose exhaustion are shown. Bar is 2 µm.

(G) Schematic of the Q-nMT bundle formation. During phase I, stable MTs (phase I MT - green) elongate from the SPB (grey). During phase II, the amount of Tub4 (cyan) increases at the SPB. In the meantime, new MTs (phase II MT - orange) elongated from the SPB and are stabilized along the phase I MTs, yet their +ends remain dynamic (dashed lines). After phase III, all MTs are stabilized (red). Nuf2 is schematized as dark blue squares.

(H) Upon glucose exhaustion, WT cells expressing mTQZ-Tub1 (green) and Nuf2-GFP (red) were pulsed treated with 30 µg/ml Noc (blue) or DMSO (grey) for 24 h. Noc or DMSO were then chased using carbon exhausted medium and cells were imaged. Each circle corresponds to MT structure length in an individual cell. The mean and SD are shown (N = 3, n > 100). Images of representative cells 2 d after the chase and representative cells 4 days after the chase are shown. Tubulin (green) was detected by immunofluorescence, actin (red) by phalloidin and DNA (blue) with DAPI. The mean Q-nMT bundle length (±SD) in the population is indicated.

To confirm the above observations, first, we followed Nuf2-GFP, a protein that localizes to the MT +end. As expected, movies showed that upon Q-nMT bundle formation initiation, Nuf2-GFP signal relocated from the SPB to the distal part of elongating Q-nMT bundles (Sup. Fig. 1E). In phase II, when cells were treated with Noc, the Nuf2-GFP signal followed depolymerizing MTs (**Fig. 1D**, left panel), testifying for the instability of phase II-MTs. In contrast, the Nuf2-GFP signal remained

immobile upon Noc treatment in phase III, as cells have fully stabilized Q-nMT bundles (**Fig. 1D**, right panel). Second, we measured the γ-tubulin (Tub4) signal at the SPB and found that Tub4 started to accumulate at the SPB at the beginning of phase I to reach a plateau at the end of phase II (**Fig. 1E** and Sup. Fig. 1F). Interestingly, the amount of Tub4 at the SPB was proportional to the thickness of the Q-nMT bundle (Sup. Fig. 1G). Finally, in order to confirm the two waves of MT elongation, we developed a strain expressing mTQZ-Tub1 from the endogenous TUB1 promoter and mRuby-TUB1 under the ADH2 promoter, a promoter that is derepressed after glucose exhaustion, as confirmed by western blot (Sup. Fig. 1H). We observed that mRuby-TUB1 was incorporated into the Q-nMT bundle only after phase I (**Fig. 1F** and Sup. Fig. 1H), confirming the existence of a second wave of MT elongation during phase II. All the above experiments led us to propose the model shown in **Figure 1G**.

Q-nMT bundle formation is an essential time-regulated process

Increasing cytoplasmic viscosity has been shown to dampen MT dynamics (Molines et al., 2022). Upon quiescence establishment, yeast cells undergo a transition from a fluid phase to a solid-like phase (Munder et al., 2016; Joyner et al., 2016) and an acidification (Jacquel et al., 2021) which could contribute to the formation of the Q-nMT bundle. Several lines of evidence suggest that these changes in physicochemical properties are not involved in Q-nMT formation. First, 4-day-old quiescent cells can simultaneously display both dynamic cytoplasmic MTs (cMTs) and a stable Q-nMT bundle (Sup. Fig. 1I and (Laporte et al., 2013)). Second, when we mimicked a fluid phase to solid-like transition in proliferating cells by artificially lowering the pH, no stable MTs were observed, whereas F-actin aggregation was induced (Sup. Fig. 1J) as expected (Peters et al., 2013). Third, 2-day-old quiescent cells exhibiting a phase III Q-nMT bundle were able to grow *de novo* dynamic cMTs after a pulse-chase Noc treatment (Sup. Fig. 1K).

Importantly, if Q-nMT bundle formation was solely dependent on physicochemical changes, this structure should be able to assemble in late quiescence. By treating cells with Noc upon glucose exhaustion, we were able to prevent the formation of the Q-nMT bundle in early quiescence (**Fig. 1H**). Strikingly, when the drug was washed out, no Q-nMT bundle assembled, even 144h after Noc removal (**Fig. 1H**). These cells had entered quiescence because they had assembled actin bodies (**Fig. 1H**, right panel), another quiescent cell-specific structure (Sagot et al., 2006). This experiment strongly suggests that Q-nMT formation is a process induced by a transient signal emitted upon glucose exhaustion.

We have previously shown that mutants unable to assemble Q-nMT bundles have reduced viability in quiescence and a reduced ability to form colonies upon exit from quiescence (Laporte et al., 2013). To establish a direct link between the absence of the Q-nMT bundle and the above phenotypes, we took advantage of our ability to conditionally prevent Q-nMT bundle formation in WT cells using Noc treatment at the onset of glucose exhaustion. As shown in Sup. Fig. 1L, in the absence of the Q-nMT bundle, WT cells lose viability in quiescence and survivors have a reduced ability to generate a progeny upon exit from quiescence. In contrast, a similar Noc treatment of cells that have already assembled a stable Q-nMT bundle (5-day-old cells) did not affect either the viability in quiescence or quiescence exit efficiency, demonstrating that Noc does not have a toxic effect *per se*. Taken together, these experiments confirm our initial findings that the Q-nMT bundle is important for both cell survival during chronological aging and quiescence exit fitness.

Steady state tubulin levels and Tub3 isotype are critical for Q-nMT bundle formation

We then focused on deciphering the molecular mechanisms involved in Q-nMT bundle formation. Yeast cells express two α-tubulin isotypes, Tub1 and Tub3. In proliferating cells, Tub1 constitutes the majority (Aiken et al., 2019; Nsamba et al., 2021; Schatz et al., 1986). In 4-day-old cells, the two α-tubulin isotypes were found embedded in the Q-nMT bundle. This was observed using two different pairs of fluorescent proteins in order to avoid any influence of the FP variants, using

both widefield and by expansion microscopy (**Fig. 2A** and Sup. Fig. 2A). Since Tub3 stabilizes MTs *in vitro* (Bode et al., 2003), it may be key for Q-nMT bundle formation. To test this hypothesis, we first analyzed the phenotype of *tub3Δ* cells. In phase II, *tub3Δ* cells displayed short MT bundles that were sensitive to Noc. In phase III, no MT bundles were detected (**Fig. 2B** and Sup. Fig. 2C). Thus, in this mutant, the MT bundles assembled during phase I were not stable and eventually collapsed. In *tub3Δ* cells, the steady-state amount of α-tubulin is significantly reduced (Sup. Fig. 2B and (Nsamba et al., 2021)). Thus, the amount of α-tubulin, but not Tub3 itself, may be important for Q-nMT bundle formation. Indeed, mutants defective in α- and β-tubulin folding, such as the prefolding complex mutants *pac10Δ*, *gim3Δ* or *yke2Δ*, or in tubulin heterodimer formation, such as *pac2Δ*, or in β-tubulin folding, such as *cin2Δ* or *cin4Δ*, all of which have a reduced amount of tubulin, were unable to assemble a Q-nMT bundle (Sup. Fig. 2D-E).

To identify the role of Tub3 *per se*, we took advantage of the "*Tub1-only*" mutant, in which the *TUB3* gene was replaced by the *TUB1* gene at the *TUB3* locus. This mutant expresses only Tub1 and has an α-tubulin level similar to WT (Sup. Fig. 2B and (Nsamba et al., 2021)). We found that "*Tub1-only*" cells have unstable Q-nMT bundles in phase II, and shorter yet stable Q-nMT bundles in phase III (**Fig. 2C** and Sup. Fig2. C). Moreover, "*Tub1-only*" Q-nMT bundles were thinner than WT Q-nMT bundles (**Fig. 2D**). Taken together, our data indicate that Tub3 is involved in MT elongation in phase II, since in the absence of this isotype, phase I MT bundles could assemble and MT bundles could get stabilized in phase III, but the second wave of MT nucleation and elongation was impaired as testified by thinner Q-nMT bundles in both phase II and III.

Kinetochores are critical for phase I but dispensable for the maintenance of Q-nMT bundles

Kinetochore components are enriched at the Q-nMT bundle +end ((Laporte et al., 2013) and Sup. Fig. 3A). We therefore tested whether kinetochore-MT attachment might play a role in Q-nMT bundle formation. First, we disrupted kinetochore-MT attachment upon glucose exhaustion using the well-established *ndc80-1* allele (Cheeseman et al., 2006; DeLuca et al., 2018; Wigge et al., 1998). As shown in **Fig. 3A**, only very short MT structures were detected in *ndc80-1* cells transferred to 37°C at the onset of quiescence entry, even after 4 days at non-permissive temperature (for control see Sup. Fig. 3B). Second, we focused on the chromosome passenger complex (CPC: Bir1/Survivin, Sli15/INCENP, Nbl1/Borealin and Ipl1/Aurora B), a complex known to regulate kinetochore-MT attachment dynamics (Cairo and Lacefield, 2020). We found that inactivation of *IPL1* upon entry into quiescence using the thermosensitive allele *ipl1-1* prevented Q-nMT bundle formation (Sup. Fig. 3C). The absence of Q-nMT bundles in cells harboring the NA-PP1 kinase-sensitive allele *ipl1-5as* indicated that the Ipl1 kinase activity was required for this process (**Fig. 3B** and Sup. Fig. 3D-E for controls). While we could not detect Ipl1 and Nbl1 in quiescent cells, we found that Sli15-GFP and Bir1-GFP localized along the Q-nMT bundle with an enrichment at the Q-nMT bundle +end (**Fig. 3C**). In 4-day-old *bir1Δ* cells, Q-nMT bundle were shorter and not fully stabilized (**Fig. 3D**). In addition, inactivation of *SLI15* upon glucose exhaustion using the thermosensitive allele *sli15-3* drastically impaired Q-nMT bundle formation (Sup. Fig. 3F). Finally, we examined the involvement of Bim1. Bim1 is a MT +end binding protein that plays a role in kinetochore MT-end on attachment (Dudziak et al., 2021; Thomas et al., 2016) and localizes along the entire Q-nMT bundle (Laporte et al., 2013). In fact, we found that the amount of Bim1 correlated with tubulin incorporation during Q-nMT bundle formation (Sup. Fig. 3G). Bim1 deletion alone has no effect on Q-nMT bundle formation even in the presence of Noc ((Laporte et al., 2013) and **Fig. 3D**). However, *bim1Δ bir1Δ* cells barely assembled MT structures, and these structures were sensitive to Noc (**Fig. 3D**). This demonstrates that in the absence of Bim1, Bir1 is critical for Q-nMT bundle stabilization in phase I. Of note, we found that the viability of *bim1Δ bir1Δ* cells in quiescence was drastically reduced (Sup. Fig. 3H). Together, these experiments show that kinetochore-MT attachments are critical for the initiation of Q-nMT bundle formation upon entry into quiescence.

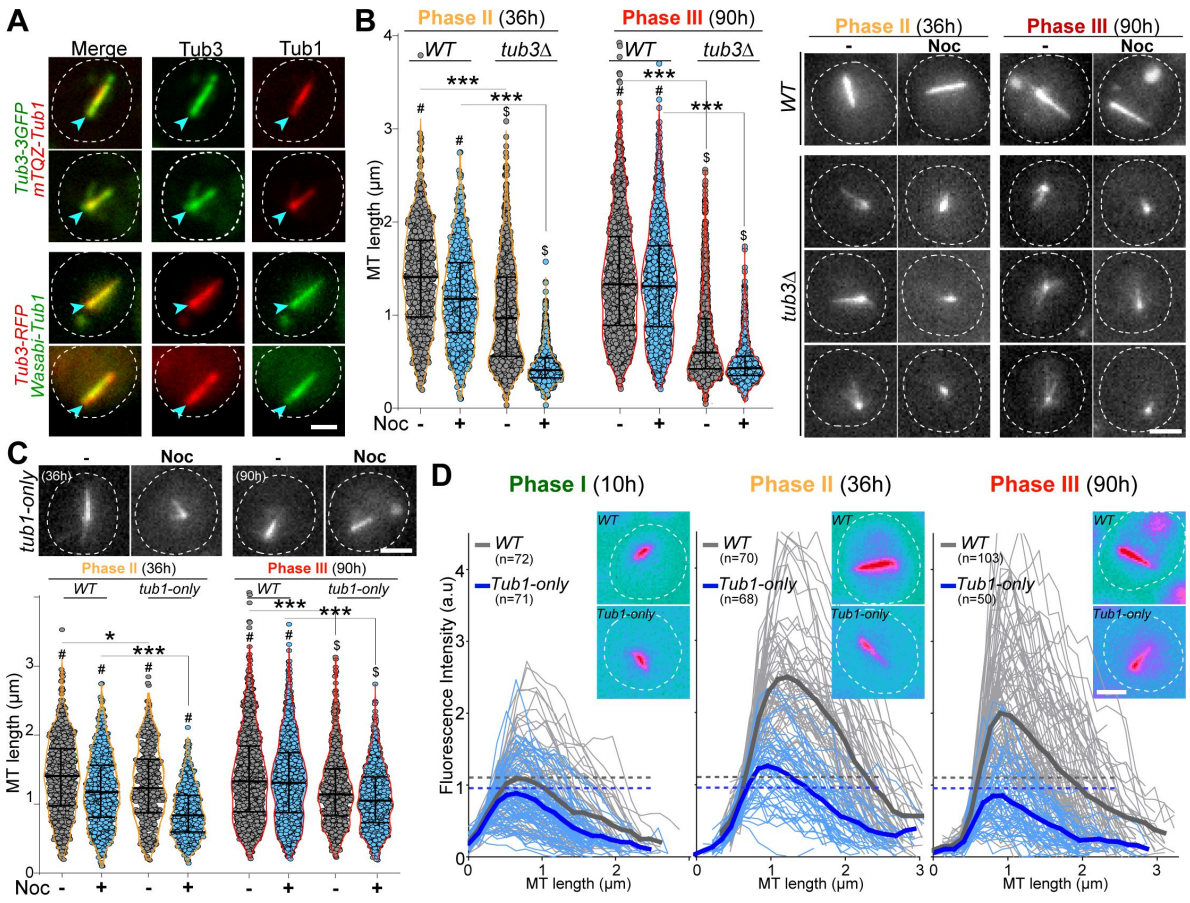

Figure 2

Q-nMT bundle formation is influenced by the alpha-tubulin amount and isotype

(A) WT cells (4 d) expressing either Tub3-3GFP (green) and mTQZ-Tub1 (red, top panel) or Tub3-RFP (red) and mWasabi-Tub1 (green, bottom panel). Blue arrowheads point to SPB, bar is 2 µm.

(B) Nuclear MT length in WT and *tub3Δ* cells expressing mTQZ-Tub1, 36 h (phase II, orange) and 90 h (phase III, red) after glucose exhaustion, treated 15 min (blue) or not (grey) with 30 µg/ml Noc. Each circle corresponds to the length of an individual MT structure, mean and SD are shown. ANOVA was used to compare inter-replicates (n > 200, N = 5); #: p-value > 0.05, $: p-value < 0.05. A student test (t-test with two independent samples) was used to compare (+) or (-) Noc data. The indicated p-values are the highest calculated among the 5 experiments; ***: p-value < 1.10^{-5}. Images of representative cells are shown, bar is 2 µm.

(C) Nuclear MT length in WT and *Tub1-only* cells expressing mTQZ-Tub1, 36 h (phase II, orange) and 90 h (phase III, red) after glucose exhaustion, treated 15 min or not with 30 µg/ml Noc. Statistical representations are as in (B). Images of representative cells are shown, bar is 2 µm.

(D) Fluorescence intensity along the Q-nMT bundle in WT (grey) and *Tub1-only* (blue) cells expressing mTQZ-Tub1 grown for 10 h (phase I), 36 h (phase II), and 90 h (phase III). Individual fluorescent intensity is shown as thin line, the mean as a bold line (n > 60 / phase), all the lines being aligned at 0,5 µm before the fluorescence intensity increase onset on the SPB side. Dashed lines indicate the maximal mean fluorescence intensity. Images in pseudo-color of representative cells are shown, bar is 2 µm.

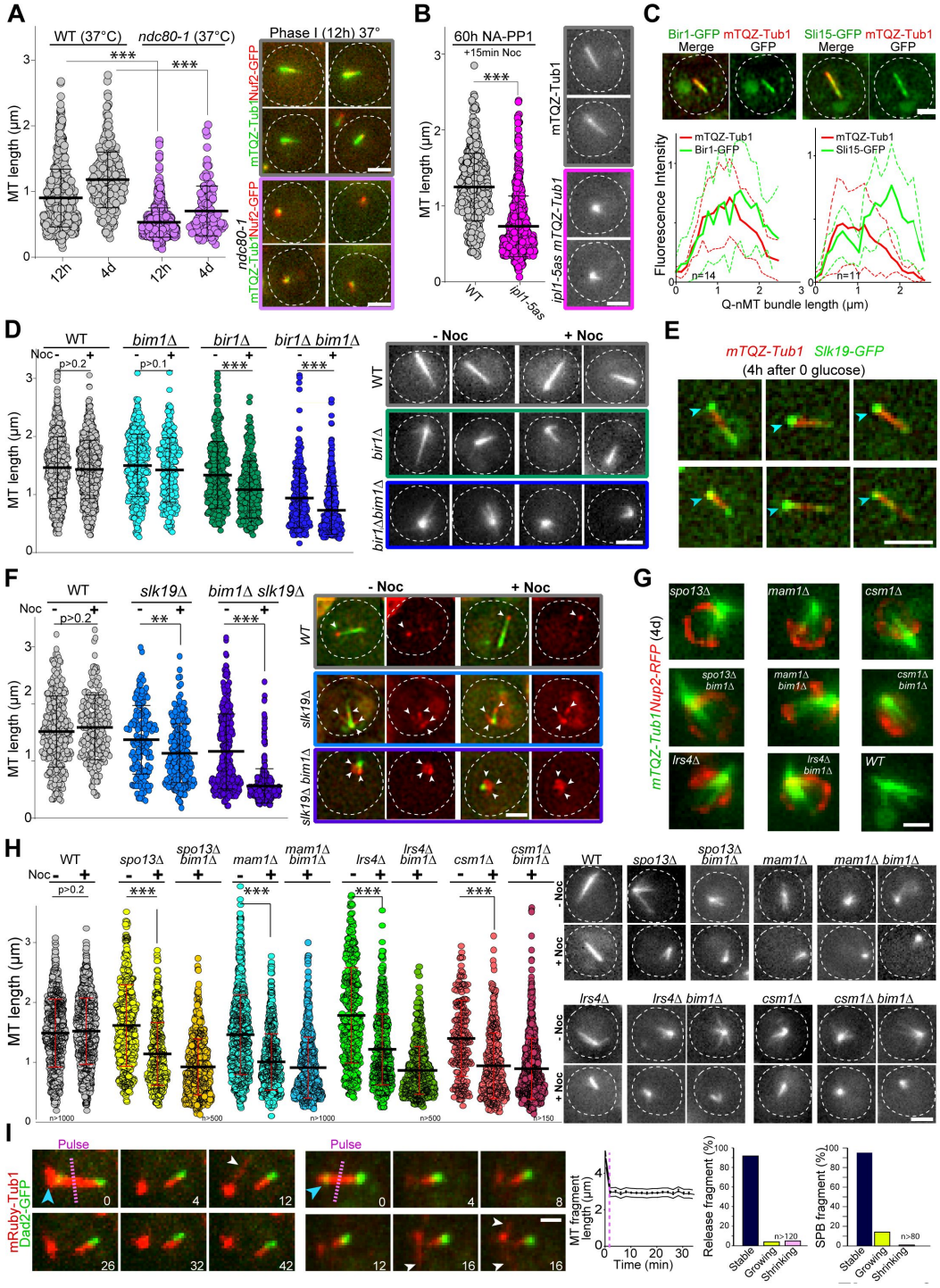
A
WT (37°C)
ndc80-1 (37°C)
MT length (µm)
12h
4d
Phase I (12h) 37°
mTQZ-Tub1Nuf2-GFP
ndc80-1
B
60h NA-PP1
+15min Noc
mTQZ-Tub1
ipl1-5as mTQZ-Tub1
WT
C
Bir1-GFP mTQZ-Tub1
Merge
GFP
Sli15-GFP mTQZ-Tub1
Fluorescence Intensity
Q-nMT bundle length (µm)
D
WT
bim1Δ
bir1Δ
bir1Δ bim1Δ
Noc
- Noc
+ Noc
E
mTQZ-Tub1 Slk19-GFP
(4h after 0 glucose)
F
slk19Δ
bim1Δ slk19Δ
G
mTQZ-Tub1Nup2-RFP (4d)
spo13Δ
mam1Δ
csm1Δ
lrs4Δ
H
spo13Δ bim1Δ
mam1Δ bim1Δ
lrs4Δ bim1Δ
csm1Δ bim1Δ
I
Pulse
mRuby-Tub1
Dad2-GFP
MT fragment length (µm)
Time (min)
Release fragment (%)
SPB fragment (%)
Stable
Growing
Shrinking

Figure 3

Kinetochore-kinetochore interactions are required for Q-nMT bundle formation

(A) Nuclear MT length distribution in WT (grey) and *ndc80-1* (violet) cells expressing mTQZ-Tub1 (green) and Nuf2-GFP (red), transferred to 37 °C upon glucose exhaustion and maintained at 37 °C for the indicated time. Cells were imaged after a 20 min Noc treatment (30 µg/ml). Each circle corresponds to the length of an individual MT structure, mean and SD are shown. A student test (t-test with two independent samples) was used to compare (**+**) or (**-**) Noc samples from the same experiment (n > 250, N = 2). The indicated p-values are the highest p-values calculated among the 2 repeated experiments. ***: p-value < 1.10^{-5}. Images of representative cells incubated 12 h at 37 °C are shown, bar is 2 µm.

(B) WT (grey) and *ipl1-5as* (pink) cells expressing mTQZ-Tub1 were treated for 60 h with 50 µM NA-PP1 after glucose exhaustion, and imaged after a 15 min Noc treatment (30 µg/ml). Same statistical representation as in (A); N = 2, n > 250. Images of representative cells are shown, bar is 2 µm.

(C) WT cells (2 d) expressing mTQZ-Tub1 (red) and Bir1-GFP or Sli15-GFP (green) were imaged. Graphs show Bir1-GFP or Sli15-GFP fluorescence intensity along normalized Q-nMT bundles (see material and method section, plain and dash lines: mean and SD respectively). Images of representative cells are shown, bar is 2 µm.

(D) Nuclear MT length distribution in cells of the indicated genotype (4 d) expressing mTQZ-Tub1 treated or not with Noc (30 µg/ml). Same statistical representation as in (A); N = 3, n > 200. Images of representative cells are shown, bar is 2 µm.

(E) WT cells expressing mTQZ-Tub1 (red) and Slk19-GFP (green) 4 h after glucose exhaustion. Blue arrowhead: SPB, bar is 2 µm.

(F) Nuclear MT length distribution in cells of the indicated genotype (4 d) expressing mTQZ-Tub1 (green) and Nuf2-GFP (red) imaged before or after Noc treatment (30 µg/ml). Same statistical representation as in (A); N = 2, n > 200. Images of representative cells are shown, white arrowheads point to Nuf2-GFP dots, bar is 2 µm.

(G) Cells of the indicated genotype (4 d) expressing mTQZ-Tub1 (green) and Nup2-RFP (red); bar is 1 µm.

(H) Nuclear MT length distribution in cells of the indicated genotype (4 d) expressing mTQZ-Tub1 treated or not with Noc (30 µg/ml). Same statistical representation as in (A); N ≥ 2, n > 200. Images of representative cells are shown, bar is 2 µm.

(I) Length variation of nuclear MT bundle fragments after laser ablation (pink dash line) in cells expressing mRuby-TUB1 (red) and Dad2-GFP (green). Time is in min. Images of representative cells are shown, blue arrowhead: SPB, white arrowhead: cMT, bar is 2 µm. Graph indicates the variation of length in released fragments (n > 120) and histograms show the % of released or SBP attached fragments that are either stable, or that shorten or grow within a 30 min period after the laser-induced breakage. Bar is 1 µm

We then hypothesized that inter-kinetochore interactions could stabilize parallel MTs embedded in the Q-nMT bundle. To test this idea, we analyzed MT organization in s*lk19Δ* cells which are defective in kinetochore clustering (Richmond et al., 2013). In quiescence, Slk19-GFP was enriched at both ends of the Q-nMT bundles (**Fig. 3E**). s*lk19Δ* cells displayed shorter and thinner MT structures that were sensitive to Noc (**Fig. 3F**). Since Bim1 has been implicated in kinetochore-kinetochore interaction, we combined s*lk19Δ* with *bim1Δ*. MT structures detected in s*lk19Δ bim1Δ* cells barely reached ≈1 µm and disappeared upon Noc treatment. In addition, in s*lk19Δ bim1Δ* cells, kinetochores localized as a rosette around the SPB (**Fig. 3F**) and s*lk19Δ bim1Δ* cell viability was severely impaired (Sup. Fig. 3H). This demonstrates that in the absence of Bim1,

Slk19 is required for MT bundling and stabilization in phase I. We then focused on monopolin (Mam1, Lrs4, Hrr25 and Csm1), a complex that is known to cross-link kinetochores (Corbett et al., 2010)). These proteins were found to be expressed in quiescent cells (Sup **Fig 3I**) and when we analyzed the phenotype of *mam1Δ, lrs4Δ* and *csm1Δ* cells in quiescence, most of them displayed short MT structures often arranged in a star-like array (**Fig. 3G-H** and Sup. Fig. 3J). As for *bir1Δ* and *slk19Δ*, the combination of *bim1Δ* with monopolin deletion worsened MT structure length and stability (**Fig. 3H**) as well as cell viability in quiescence (Sup. Fig. 3H). Furthermore, cells deleted for *SPO13*, a gene encoding a protein involved in monopolin recruitment to kinetochores (Lee et al., 2004) showed similar phenotypes (**Fig. 3G-H** and Sup. Fig. 3H). Collectively, these experiments demonstrate that inter-kinetochore interactions are critical for Q-nMT bundle assembly.

Finally, we investigated whether kinetochore-MT interactions were required for the stability of the Q-nMT bundle once it is formed. In 5-day-old WT cells, we used a UV-pulsed laser to break the Q-nMT bundle into two pieces. In most cases, the length of both the released fragment and the fragment attached to the SPB remained constant, with the presence of dynamic cMTs after laser ablation testifying for cell viability (**Fig. 3I**, Sup. Fig. 3K). In contrast, as expected form previous studies (Khodjakov et al., 2004; Zareiesfandabadi and Elting, 2022), in proliferating cells, dynamic anaphase spindles promptly disassembled after the laser-induced breakage (Sup. Fig. 3L). This indicates that once Q-nMT bundles are formed, they do not require MT-kinetochore interaction to be maintained. Accordingly, inactivation of Ndc80 (Sup **Fig. 3B**) or Ipl1 (Sup. Fig. 3M) in cells that are already in quiescence had no effect on the Q-nMT bundle maintenance. Thus, once formed, Q-nMT stability is established and maintained throughout its length.

Each phase of Q-nMT bundle formation requires specific kinesins

To further dissect the molecular mechanism of Q-nMT bundle formation, we focused on kinesins. Kar3 is a kinesin that, in complex with its regulator Cik1, can generate parallel MT bundles from a MT organizing center (MTOC) both *in vitro* and in proliferating cells (Manning et al., 1999; Mieck et al., 2015; Molodtsov et al., 2016). In quiescence, we found that Kar3-3GFP localized to the SPB, but also as dots along the Q-nMT bundle (**Fig. 4A**). In 4-day-old *kar3Δ* cells, the majority of the detected MT structures were extremely short compared to WT (**Fig. 4B**, for control without Noc see Sup **Fig. 4A**). Similar results were obtained in *cik1Δ* but not in *vik1Δ* cells, which lack the alternative Kar3 regulators (**Fig. 4B**). Thus, the Kar3/Cik1 complex is required for phase I.

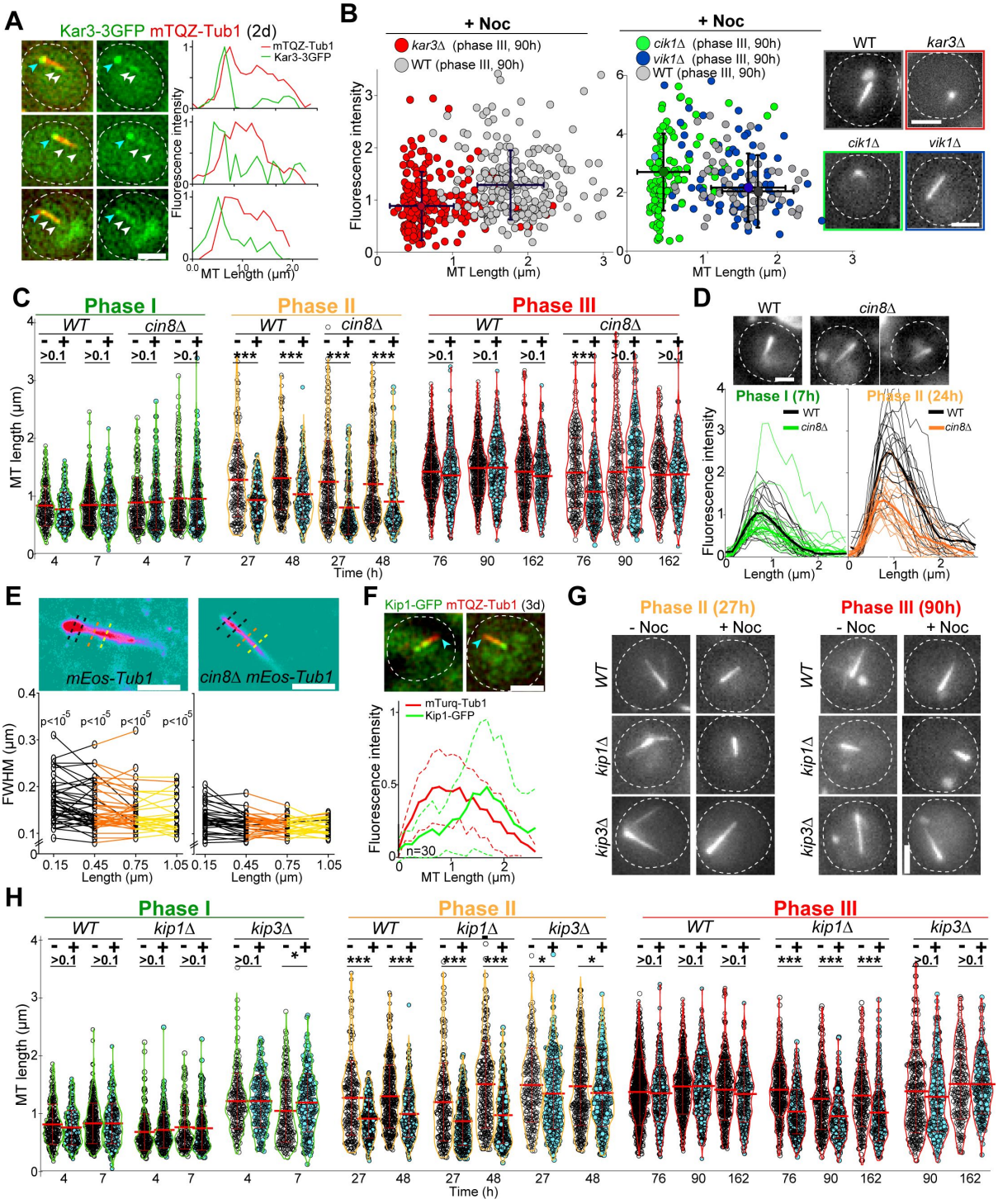
A
Kar3-3GFP mTQZ-Tub1 (2d)
mTQZ-Tub1
Kar3-3GFP
Fluorescence intensity
MT Length (µm)
B
+ Noc
kar3Δ (phase III, 90h)
WT (phase III, 90h)
+ Noc
cik1Δ (phase III, 90h)
vik1Δ (phase III, 90h)
WT (phase III, 90h)
WT
kar3Δ
cik1Δ
vik1Δ
Fluorescence intensity
MT Length (µm)
C
Phase I
Phase II
Phase III
WT
cin8Δ
MT length (µm)
Time (h)
D
WT
cin8Δ
Phase I (7h)
Phase II (24h)
Fluorescence intensity
Length (µm)
E
mEos-Tub1
cin8Δ mEos-Tub1
FWHM (µm)
Length (µm)
F
Kip1-GFP mTQZ-Tub1 (3d)
mTurq-Tub1
Kip1-GFP
n=30
Fluorescence intensity
MT Length (µm)
G
Phase II (27h)
Phase III (90h)
- Noc
+ Noc
WT
kip1Δ
kip3Δ
H
Phase I
Phase II
Phase III
WT
kip1Δ
kip3Δ
MT length (µm)
Time (h)

Figure 4

Each phase of Q-nMT formation requires a specific kinesin

(A) Images of representative WT cells (2 d) expressing Kar3-3GFP (green) and mTQZ-Tub1 (red) and corresponding fluorescence intensity along normalized Q-nMT bundles (see material and method section), bar is 2 µm.

(B) Morphometric Q-nMT bundle properties distribution in 4 d WT (grey), *kar3Δ* (red), *vik1Δ* (blue), and *cik1Δ* cells (green) expressing mTQZ-Tub1 after Noc treatment (30 µg/ml) – see Sup. Fig. 4A for the control without Noc. Each circle corresponds to an individual Q-nMT bundle. Black crosses are mean and SD. Images of representative cells are shown, bar is 2 µm.

(C) Nuclear MT length distribution in WT and *cin8Δ* cells expressing mTQZ-Tub1 treated (**+**) or not (**-**) with 15 min Noc (30 µg/ml). Each circle corresponds to the length of an individual MT structure, mean and SD are shown. A student test (t-test with two independent samples) was used to compare (**+**) or (**-**) Noc samples from the same experiment (n > 250, N = 2). The indicated p-values are the highest p-values calculated among the 2 repeated experiments. ***: p-value < 1.10^{-5}.

(D) Fluorescence intensity along Q-nMT bundles in WT and *cin8Δ* cells expressing mTQZ-Tub1 7 h and 24 h after glucose exhaustion. Thin line: intensity from an individual cell; bold line: mean intensity (n > 60 / phase). Images of representative cells are shown, bar is 2 µm.

(E) WT and *cin8Δ* cells expressing mEOS3.2-Tub1 were imaged using PALM. Images in pseudo-colors of representative cells are shown. Full width at half maximum (FWHM) was measured at the indicated distance from the SPB. Each line in the bottom graphs corresponds to a single cell; p-value between WT and *cin8Δ* are indicated (unpaired t-test). Bar is 2 µm.

(F) Images of representative WT cells (3 d) expressing Kip1-GFP (green) and mTQZ-Tub1 (red). Graphs show fluorescence intensity along normalized Q-nMT bundles (plain and dash lines: mean and SD respectively). Bar is 2 µm, blue arrowhead: SPB.

(G) Representative images of WT, *kip1Δ* and *kip3Δ* cells expressing mTQZ-Tub1 treated (**+**) or not (**-**) with 15 min Noc (30 µg/ml), Bar is 2 µm.

(H) Nuclear MT length distribution in WT, *kip1Δ* and *kip3Δ* cells expressing mTQZ-Tub1 treated (**+**) or not (**-**) 15 min with Noc (30µg/ml). Legend is the same as in (C); n > 250; *: p-value < 1.10^{-3}; ***: p-value < 1.10^{-6}. MT mean length and SD are indicated.

Cin8 is a kinesin-5 that cross-links MTs (Bodrug et al., 2020; Pandey et al., 2021; Singh et al., 2018), and as such, could play a role in stabilizing Q-nMT bundles. Cin8 was barely detectable in quiescent cells (Sup. Fig. 4B) and *cin8Δ* cells assembled Q-nMT bundles that were thinner than in WT cells (**Fig. 4C-E**). However, these thinner bundles were stabilized in phase III (**Fig. 4C** and Sup. Fig. 4C-D). Taken together, these results strongly suggest that Cin8 is required for MT nucleation and/or elongation in phase II but not for stabilization in phase III.

Yeast have an additional kinesin-5 called Kip1 (Fridman et al., 2013). In quiescence, most of the Kip1-GFP signal was observed at the Q-nMT bundle +end (**Fig. 4F**). In *kip1Δ* cells, phase I was slightly delayed. In phase III, while as thick as WT Q-nMT bundles, MT bundles detected in *kip1Δ* cells were not fully stabilized (**Fig. 4G-H** and Sup. Fig. 4E). These data demonstrate that Kip1 is required for Q-nMT bundle stabilization in phase III. Of note, in phase I and II, Q-nMT bundles were slightly longer in cells deleted for the kinesin-8 Kip3, a MT depolymerase ((Fukuda et al.,

2014), **Fig. 4 G-H** and Sup. Fig. 4G), but have a WT morphology in cells deleted for Kip2, a kinesin that stabilizes cytoplasmic MTs ((Hibbel et al., 2015); Sup. Fig. 4F-G). Taken together our results demonstrate that each phase of Q-nMT bundle assembly involves specific kinesins.

SPB duplication/separation requires Q-nMT bundle disassembly

Finally, we questioned the molecular mechanism of Q-nMT bundle disassembly upon exit from quiescence. We first found that cycloheximide prevented Q-nMT bundle disassembly indicating that this process requires *de novo* protein synthesis (**Fig. 5A**). Then we measured Q-nMT bundle thickness upon depolymerization, and found that while Q-nMT bundles shortened, they did not become thinner (**Fig. 5B**). In agreement, Nuf2-GFP clusters found at the Q-nMT bundle +end moved back to the SPB while the Nuf2-GFP clusters localized along the Q-nMT bundle remained immobile until they are reached by the +end-associated clusters (Sup. Fig. 5A). This shows that not all MT +ends started depolymerizing at the same time, and that longer MTs depolymerized first. This finding is consistent with our model in which MTs are cross-linked along the entire length of the Q-nMT bundle.

Since Kip3 is the only well-characterized yeast MT depolymerase, we examined Q-nMT bundle disassembly in *kip3Δ* cells and found that it was drastically delayed (**Fig. 5C**, Sup. Fig. 5B), yet the overall depolymerization rate remained unaffected (Sup. Fig. 5B, left panel). In fact, we found that in WT cells, Kip3 needs to be resynthesized upon exit from quiescence (Sup. Fig. 5C). We searched for proteins that might be involved in Q-nMT bundle disassembly together with Kip3. Among the proteins required for mitotic spindle disassembly, we found that inactivation of *CDC14*, *CDC15*, *CDH1*, *DCC1*, and *TOR1* had no effect on Q-nMT bundle disassembly, as did the inactivation of Ipl1 or proteins involved in kinetochore-MT attachment (Sup. Fig. 5D-G). The only additional actor we found was She1, a dynein regulator (Bergman et al., 2012), whose deletion strongly exacerbated the *kip3Δ* phenotype (**Fig. 5C**, Sup. Fig. 5H). Thus, Q-nMT bundle disassembly does not rely on the canonical mitotic spindle disassembly machinery, but rather specifically requires Kip3 and She1.

Importantly, when we followed quiescence exit at the single cell level, depolymerization of the Q-nMT bundle always preceded SPB duplication/separation (**Fig. 5A**), in both WT and in *kip3Δ* cells (Sup. Fig. 5B, right panel). When we severely impeded Q-nMT bundle disassembly using *kip3Δ she1Δ*, we found that SPB separation was greatly delayed (**Fig. 5D-F**, Sup. Fig. 5I-K). Besides, the growth rate of *kip3Δ she1Δ* cells during proliferation is the same as WT cells (Sup. Fig. 5I), and upon quiescence exit, these mutant cells disassembled actin bodies as fast as WT cells (Sup. Fig. 5K), demonstrating that *kip3Δ she1Δ* cells were not impaired in sensing quiescence exit signals. These observations suggest that upon exit from quiescence, the Q-nMT bundle has to be disassembled prior to SPB duplication/separation.

Discussion

Our results shed light on the precise temporal sequences that generate a Q-nMT bundle upon quiescence establishment in yeast. From bacteria to human stem cells, changes in cell physicochemical properties are known to accompany the establishment of quiescence. Among these modifications, cellular volume reduction increases molecular crowding (Joyner et al., 2016), and pH acidification both increases viscosity and causes changes in macromolecule surface charges (Charruyer and Ghadially, 2018; Jacquel et al., 2021; Munder et al., 2016; Persson et al., 2020). Much evidence suggests that these modifications act as triggers for the auto-assembly of several types of enzyme-containing granules (Munder et al., 2016; Petrovska et al., 2014; Rabouille and Alberti, 2017), or complex structures such as P-bodies and Proteasome Storage Granules (Peters et al., 2013; Jacquel et al., 2021; Currie et al., 2023). Recently, Molines and colleagues demonstrated that cytoplasmic viscosity modulates MT dynamics *in vivo*

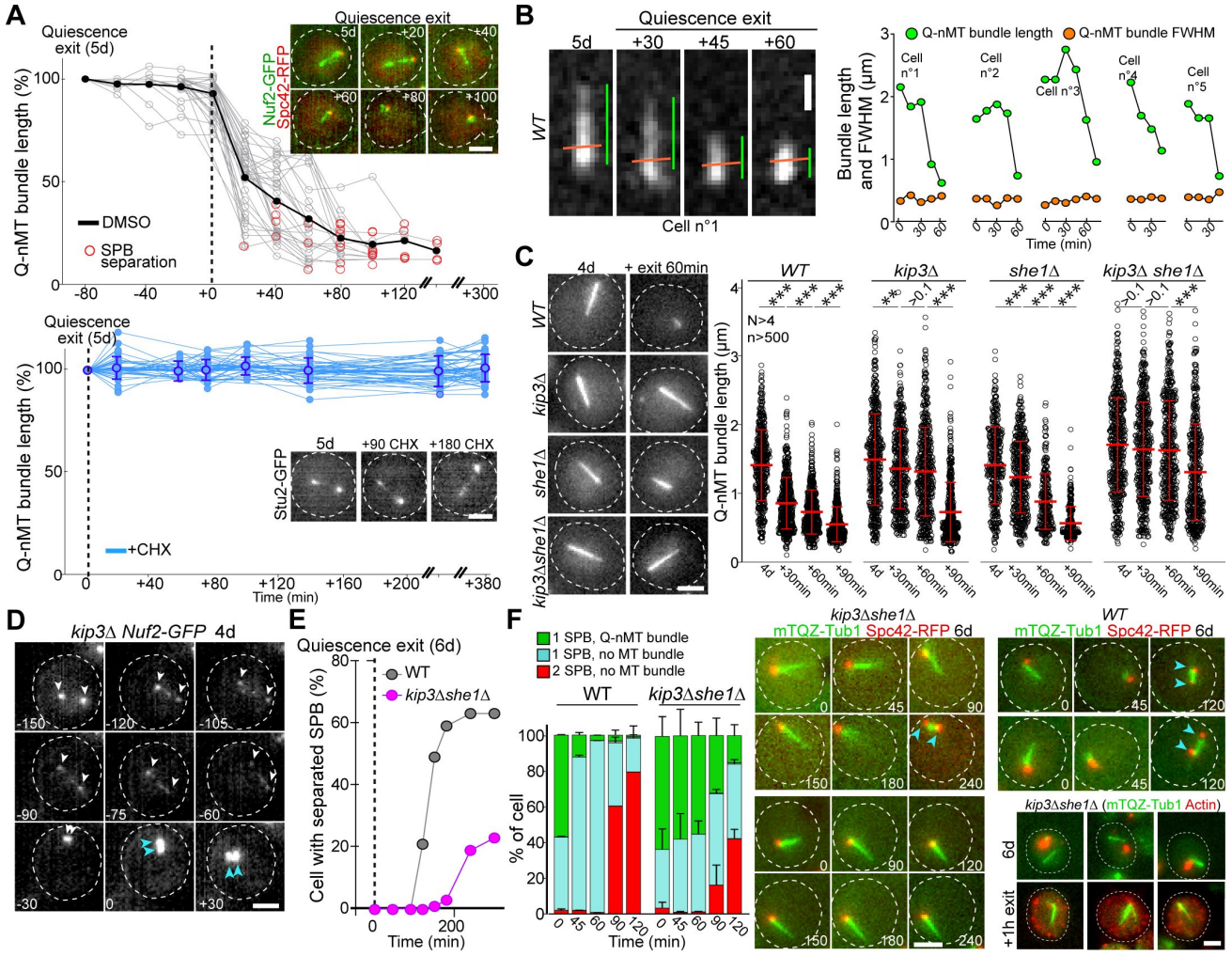

Figure 5

Q-nMT bundle disassembly always occurs before SPB separation upon quiescence exit

(A) WT cells expressing Spc42-RFP (red) and Nuf2-GFP (green) (5 d) were re-fed on an YPDA microscope pad. Individual Q-nMT bundles were measured in cells treated with DMSO (top panel, Nuf2-GFP, n=33) or with CHX (bottom panel, Stu2-GFP, n=49). Each line corresponds to an individual cell. In the upper panel, time was set to zero at the onset of MT bundle depolymerisation. In the lower panel, time was set to zero when cells were deposited on the agarose pad, bar is 2 µm.
(B) Q-nMT bundle length (green) and fluorescence intensity at full width half maximum (FWHM - orange) were measured upon quiescence exit in WT cells (5 d) expressing mTQZ-Tub1. Representative example of shrinking Q-nMT bundle is shown on the left, bar is 1 µm.
(C) Cells of the indicated genotype expressing mTQZ-Tub1 were grown for 4 d, and re-fed. Q-nMT bundle length was measured at the indicated time points, 15 min after a Noc treatment (30 µg/ml), to remove all dynamic cMTs. Each circle corresponds to a single cell. MT mean length and SD are indicated. A student test (t-test with two independent samples) was used to compare samples from the same experiment (n > 250, N = 4). The indicated p-values are the highest p-value calculated among the 4 repeated experiments. ***: p-value < 1.10^{-5}. MT mean length and SD are indicated. Images of representative 4-day-old cells of the indicated genotype expressing mTQZ-Tub1 before and 60 min after quiescence exit are shown, bar is 2 µm.
(D) Representative images of a *kip3Δ* cell expressing Nuf2-GFP upon quiescence exit. Blue and white arrowheads: SPBs and Q-nMT bundle extremities respectively, bar is 2 µm.
(E) Percentage of 6-day-old cells expressing Spc42-mRFP1 with separated SPB as a function of time upon quiescence exit (n > 200).
(F) WT and *kip3Δshe1Δ* cells (6 d) expressing Spc42-mRFP1 (red) and mTQZ-Tub1 (green) were re-fed on a YPDA microscope pad. Percentage of cells with a single SBP with or without Q-nMT bundle or with duplicated SPBs were scored (N = 4, n > 200), SD are indicated. Images of representative cells are shown, bar is 2 µm. Right bottom panel: actin (phalloidin staining, red) in *kip3Δ she1Δ* cells (6 d) expressing mTQZ-Tub1 (green) before and 1 h after quiescence exit.

Our results shed light on the precise temporal sequences that generate a Q-nMT bundle upon quiescence establishment in yeast. From bacteria to human stem cells, changes in cell physicochemical properties are known to accompany the establishment of quiescence. Among these modifications, cellular volume reduction increases molecular crowding (Joyner et al., 2016), and pH acidification both increases viscosity and causes changes in macromolecule surface charges (Charruyer and Ghadially, 2018; Jacquel et al., 2021; Munder et al., 2016; Persson et al., 2020). Much evidence suggests that these modifications act as triggers for the auto-assembly of several types of enzyme-containing granules (Munder et al., 2016; Petrovska et al., 2014; Rabouille and Alberti, 2017), or complex structures such as P-bodies and Proteasome Storage Granules (Peters et al., 2013; Jacquel et al., 2021; Currie et al., 2023). Recently, Molines and colleagues demonstrated that cytoplasmic viscosity modulates MT dynamics *in vivo* (Molines et al., 2022). Here, we showed that the formation of the Q-nMT bundle does not depend on changes in the physicochemical properties that cells experience at the onset of quiescence establishment (Sup. Fig. 1). In fact, dynamic cMTs and a stable Q-nMT bundle can be observed simultaneously in a quiescent cell (Sup. Fig. 1I), while physicochemical properties evolve in parallel in both the nucleus and the cytoplasm (Joyner et al., 2016). Importantly, cellular volume reduction, pH acidification and increased viscosity are observed within minutes upon glucose starvation (Joyner et al., 2016) whereas the Q-nMT bundles require a couple of days to be fully assembled (**Fig. 1**). Furthermore, Q-nMT bundle formation cannot be delayed in time (**Fig. 1H**), and thus likely depends on a transient signal emitted upon glucose depletion. We speculate that the SPB may act as a platform that integrates this signal, and transfers it to the MT machinery in order to assemble a stable MT structure.

As it is required for the onset of Q-nMT bundle formation (**Fig. 3B**), the CPC component Aurora B/Ilp1, a kinase that plays a key role at the MT-kinetochore interface in response to the tension status, could be one of the targets of the aforementioned nutritional signal. In parallel, upon quiescence establishment, chromosome hyper-condensation (Guidi et al., 2015; Rutledge et al., 2015) could modify the tension at the kinetochore/MT interface and, as such, could contribute to the initiation of phase I (**Fig. 6b**). Besides, Bim1 has also been implicated in MT-kinetochore attachment (Dudziak et al., 2021; Akhmanova and Steinmetz, 2015). Although its deletion alone has no effect on Q-nMT bundle formation, its role becomes critical for phase I when kinetochore-MT interactions are already destabilized by the absence of other CPC components, other than Ipl1, such as Bir1 (**Fig. 3D**). Taken together, these observations suggest that kinetochore-MT interactions are essential for phase I initiation, as confirmed by the absence of Q-nMT bundle in the *ndc80-1* mutant (**Fig. 3A**).

In phase I, SPB-anchored MTs elongate and are concomitantly stabilized (**Fig. 1 A-C**). This step requires the kinesin-14 Kar3 and its regulator Cik1 (**Fig. 4B**). During mating (Molodtsov et al., 2016), and in early mitosis, when half-spindles form (Kornakov et al., 2020), Kar3/Cik1, together with Bim1, align and cross-link growing MTs along existing MTs, thereby promoting the organization of MTs into parallel bundles. In mitosis however, the kinesin-14/EB1 complex promotes MT dynamics (Kornakov et al., 2020). It remains to be determined whether the robust MT stabilization in phase I depends on the modification of the kinesin-14/EB1 complex properties and/or on additional specific cross-linker(s) (**Fig. 6c**).

In quiescence, deletion of either Monopolin or *SLK19* results in the formation of short, shattered and flared MT structures, phenotypes that are exacerbated by the deletion of *BIM1* (**Fig. 3F-H**). Since Monopolin and Slk19 are involved in kinetochore clustering (Plowman et al., 2019; Rabitsch et al., 2003; Tóth et al., 2000; Lee et al., 2004; Mittal et al., 2019; Movshovich et al., 2008; Richmond et al., 2013; Zeng et al., 1999), we speculate that kinetochore-kinetochore interaction may not only help prevent depolymerization of individual MTs, but also constrain elongating phase I MTs and facilitate their concomitant cross-linking (**Fig. 6d**).

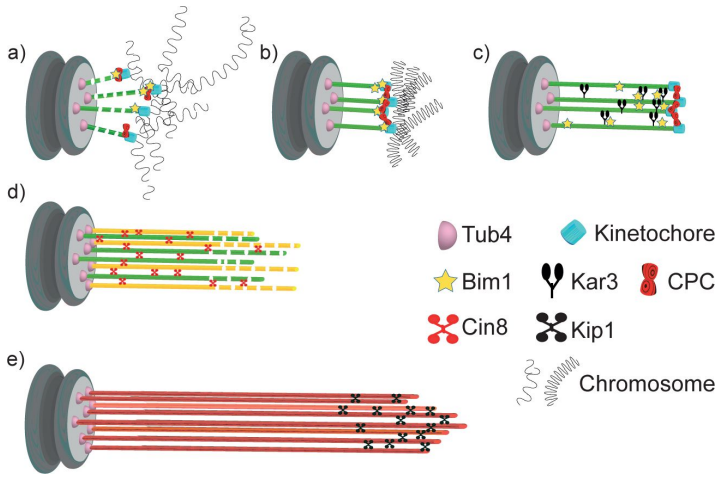

Figure 6

Model for Q-nMT bundle assembly

(a) In G1, the nucleus is in a Rabl-like configuration. (b) Upon quiescence establishment, chromosomes get condensed. MT-kinetochore interaction and Ilp1 are required for the onset of phase I. (c) Kar3 and its regulator Cik1 are essential to initiate Q-nMT bundle elongation. Although deletion of *BIM1* has no effect, it becomes critical for phase I if kinetochore-MT interactions are destabilized by the absence of Chromosome Passenger Complex components. Kinetochore clustering by the monopolin complex and Slk19 is needed to maintain MT bundling while phase I MTs elongate. During phase I, Tub4 (ɣ-Tubulin) accumulates at the SPB. (d) In phase II, a second wave of MT nucleation and elongation occur. Phase II MTs are concurrently stabilized along pre-existing phase I MTs, in a Cin8-dependent manner. Phase I and phase II MT +ends (>1 µm) remain dynamic until the full-length Q-nMT bundle stabilization is reached via the action of Kip1, about 2 days after glucose exhaustion (e).

With the initiation of phase I, Tub4 begins to accumulate at the SPB to enable the second wave of MT nucleation observed in phase II. As phase II MTs elongate, they are simultaneously stabilized along pre-existing phase I MTs (**Fig. 6d**). This step relies on the kinesin-5/Cin8 as Q-nMT bundles assembled in *cin8Δ* cells are thinner than WT Q-nMT bundles (**Fig. 4C-E**). Intriguingly, *in vitro*, the monomeric form of the vertebrate kinesin-5, Eg5, promotes MT nucleation and stabilizes lateral tubulin-tubulin contacts (Chen et al 2019). We assume that in the absence of Cin8, either nucleation of phase II MTs cannot occur, or phase II MTs can elongate, but cannot be cross-linked and stabilized to a pre-existing phase I MT(s) as they grow, and thus rapidly depolymerize. Absence of bundle thickening in phase II is also observed in the "*Tub1-only*" mutant *i.e.* in the absence of Tub3. Tubulin isotypes or tubulin PTMs are known to promote the recruitment of specific kinesins and thereby modify MT properties, see for example (Sirajuddin et al., 2014; Peris et al., 2009; Dunn et al., 2008). Could Tub3 be important for Cin8 recruitment or function during phase II?

Following phase II, MTs elongate, but their distal parts (>1 µm) are not yet stable (**Fig. 1A**). Stabilization of full-length Q-nMT bundles is achieved approximately 4 days after glucose exhaustion. This step depends on the kinesin-5/Kip1 (**Fig. 4G-H** and Sup. Fig. 4E) which is essential for cross-linking and stabilizing elongating MTs during phase III (**Fig. 6e**). Accordingly, we observed a Kip1 enrichment at the Q-nMT bundle +ends (**Fig. 4F**). Thus, consistent with their ability to form homo-tetramers capable of cross-linking (Acar et al., 2013; Kapitein et al., 2005; Scholey et al., 2014; Weinger et al., 2011) and stabilizing parallel MTs (Kapitein et al., 2005; Shimamoto et al., 2015; Yukawa et al., 2020) in addition to their role of sliding anti-parallel MTs, the two yeast kinesins 5 are essential for Q-nMT bundle formation. However, in quiescence, as well as in mitosis, Kip1 and Cin8 have non-equivalent functions (Roostalu et al., 2011; Shapira and Gheber, 2016).

Thus far, our results indicate that the mechanism of Q-nMT bundle formation is distinct from that of mitotic spindle assembly. Similarly, we show that Q-nMT bundle disassembly does not involve the same pathway as mitotic spindle disassembly as it involves Kip3 (**Fig. 5C**) but is independent of the anaphase-promoting complex and Aurora B/Ipl1 (Sup. Fig. 5D-G). Interestingly, the longest MTs begin to depolymerize from their +ends first. Then, when they reach the +ends of shorter MTs, the shorter ones proceed to depolymerize alongside them (Sup. Fig. 5A). This cooperative behavior has been observed *in vitro* within parallel MT bundles (Laan et al., 2008). Our data demonstrate that such a comportment does exist *in vivo*.

Finally, our data indicate that the Q-nMT bundle is required for the survival of WT cells in quiescence. While we do not yet know why this structure is important for chronological aging, it is clear that the presence of the Q-nMT bundle modifies the organization of the nucleus (Laporte et al., 2013; Laporte and Sagot, 2014; Laporte et al., 2016). Since chromatin organization influences gene expression, one hypothesis could be that the presence of the Q-nMT bundle is required for the expression of genes necessary for cell survival in quiescence. Another attractive hypothesis is that the Q-nMT bundle could be the yeast analog of the mammalian primary cilium. Indeed, these two structures are formed upon proliferation cessation, they are both composed of highly stable parallel MTs, their formation involves MT motors, and they are both templated from the centriole/SPB. More importantly, we show here that Q-nMT disassembly is required to allow SPB separation upon exit from quiescence (**Fig. 5**). Thus, the Q-nMT bundle disassembly may control reentry into the proliferation cycle, just as the primary cilium does in ciliated mammalian cells (Goto et al., 2017; Kim and Tsiokas, 2011).

Materiel and Methods

Yeast strains, plasmids and growth conditions

All the strains used in this study are isogenic to BY4741 (*mat a, leu2Δ0, his3Δ0, ura3Δ0, met15Δ0)* or BY4742 (*mat alpha, leu2Δ0, his3Δ0, ura3Δ0, lys2Δ0),* available from GE Healthcare Dharmacon Inc. (UK), except for **Fig. 2**, in which strains of the S288c background were used (Nsamba et al., 2021) and Sup. Fig. 1F in which the W303 background was used. BY strains carrying GFP fusions were obtained from ThermoFisher Scientific (Waltham, MA, USA). Integrative plasmids p*Tub1-mTurquoise2-Tub1*, p*Tub1-wasabi-Tub1*, p*Tub1-mRUBY2-Tub1*, p*Tub1-mEOS2-Tub1* were a generous gift of Wei-Lih Lee (Markus et al., 2015). The strain expressing SPC42-mRFP1 is a generous gift from E. O'Shea (Huh et al., 2003). The strain expressing TUB4-mTQZ is a generous gift of S. Jaspersen (Burns et al., 2015). The *Ipl1-5as* is a generous gift from A. Marston. *Ipl1-1, ndc80-1* and *Sli15-3* are a generous gift from C. Boone. Three copies of eGFP in tandem were integrated at the 3' end of *DAD2*, *TUB3* or *KAR3* endogenous loci respectively. Plasmids for expressing Nup2-RFP (p3695) or Bim1-3xGFP (p4587) from the endogenous locus were described in (Laporte et al., 2013).

For **Fig. 1F**, *pHIS3:mTurquoise2-Tub1+3'UTR::LEU2* was integrated at the *TUB1* locus, then a pRS303-*ADH2p-mRuby2-Tub1* was integrated at the *HIS3* locus. To generate this plasmid, the *ADH2* promoter was amplified from yeast genomic DNA flanked with NotI and SpeI restrictions sites and inserted in pRS303. The mRuby2-Tub1+3'UTR, including the 116-nucleotide intron and 618 nucleotides downstream of the stop codon was cloned between SpeI/SalI sites.

Yeast cells were grown in liquid YPDA medium at 30 °C in flasks as described previously in (Sagot et al., 2006) except for experiments using thermosensitive strains, where cells were first grown at 25 °C then shifted at 37 °C for the indicated time before imaging.

The experiment in Sup. Fig. 1J was performed as described in (Orij et al., 2009; Peters et al., 2013). In brief, proliferating cells were transferred at an OD_{600nm} of 0.5 in Hepes buffer (25 mM Hepes, pH 7.4, 200 mM KCl, 1 mM $CaCl_2$, and 2 % dextrose), buffered either at pH 4 or 7.5, in the presence of 100 µM CCCP (Sigma-Aldrich). After 150 min 30 °C shaking, cells were imaged (for mTQZ-Tub1) or fixed and stained using Alexa Fluor 568–phalloidin (Invitrogen) as described (Sagot et al., 2006).

For live cell imaging, 2 µL of the cell culture were spotted onto a glass slide and immediately imaged at room temperature.

For quiescence exit, cells were first incubated 2-3 min in liquid YPD and then 2 µL were spread onto a 2 % agarose microscope pad containing YPD. Individual cells were imaged every hour, up to 6 or 12 h at 21°C. For quiescence exit in presence of cycloheximide (**Fig. 5A**), cells were pre-incubated 30 min in the presence of the drug prior to quiescence exit. Cycloheximide was used at 180 µM (Sigma-Aldrich), Nocodazole was used at 30 µg/mL (7.5 µM) (Sigma-Aldrich), NA-PP1 was used at 50µM (Sigma-Aldrich).

Fluorescence Microscopy

Cells were observed on a fully-automated Zeiss 200M inverted microscope (Carl Zeiss, Thornwood, NY, USA) equipped with an MS-2000 stage (Applied Scientific Instrumentation, Eugene, OR, USA), a Lambda LS 300 Watt xenon light source (Sutter, Novato, CA, USA), a 100X 1.4NA Plan-Apochromat objective, and a 5 position filter turret. For RFP and mRuby2 imaging we used a Cy3 filter (Ex: HQ535/50 nm – Em: HQ610/75 nm – BS: Q565 nm lp). For GFP imaging, we used a FITC filter (excitation, HQ487/25 nm; emission, HQ535/40 nm; beam splitter, Q505 nm lp). For mTurquoise2 imaging we used a DAPI filter (Ex: 360/40 nm – Em: 460/50 nm– BS: 400 nm). All the filters are from

Chroma Technology Corp. Images were acquired using a CoolSnap HQ camera (Roper Scientific, Tucson, AZ, USA). The microscope, camera, and shutters (Uniblitz, Rochester, NY, USA) were controlled by SlideBook software 5.0. (Intelligent Imaging Innovations, Denver, CO, USA).

For PALM (**Fig. 4E**) a Nikon Ti-Eclipse equipped with iLas2 TIRF arm, laser diodes (405, 488, 532, 561, 642 nm), a 100x 1.49 oil (TIRF) objective connected to a EMCCD Camera Photometrics Evolve was used.

Immunofluorescence was done as in (Laporte et al., 2016) and actin AlexaFluor Phalloidin (Invitrogen) staining as in (Sagot et al., 2006).

For expansion microscopy (Sup Fig. 2A and 3A), spheroplasts were obtained as described in (Laporte et al., 2016). After washing in 10 mg/mL NaBH4 in PEMS for 10 min, spheroplasts were seeded on 12 mm round poly-L-lysine coated coverslips, washed twice for 30 min in 100 µL PEM-BAL (PEM + 1% BSA) and incubated with the primary antibodies (anti-GFP from mouse; Roche, ref. 11814460001, 1/50; anti-alpha-tubulin from rat; YOL1/34, Abcam, ref. Ab6161, 1/100) for 1 hour at 37°C. Cells were then washed three times in PEM-BAL and incubated with the secondary antibodies (Goat anti-mouse AlexaFluor®488 1/200 and Donkey anti-rat AlexaFluor®555; A11029 and A21434 respectively, ThermoFisher Scientific, Waltham, MA) for 45 min at 37 °C. Cells were then washed three times with PBS. Cells were processed for Expansion Microscopy as previously described in (Bahri et al., 2021). Spheroplasts were incubated for 10 min in 0.25 % GA in PBS, washed in PBS three times for 5 min, and processed for gelation. A drop of 100 µL of ExM MS (8.625% (wt/wt) SA, 2.5% (wt/wt) AA, 0.15 % (wt/wt) BIS, 2 M NaCl in 1× PBS) was placed on the chilled parafilm, and coverslips were put on the drop with cells facing the solution and incubated for 3 min. Then the coverslips were transferred to 35 µL of ExM MS supplemented with 0.2 % APS and 0.2 % TEMED, with the initiator (APS) added last. Gelation proceeded for 3 min on ice, and samples were incubated at 37 °C in a humidified chamber in the dark for 1 h. Then coverslips with attached gels were transferred into a six-well plate for incubation in 2 mL of digestion buffer (1× TAE buffer, 0.5% Triton X-100, 0.8 M guanidine hydrochloride, pH ~8.3) supplemented with DAPI (1 µg/mL) for 10-15 min at 37 °C, until the gels detached. Fresh proteinase K at 8 units/mL was then added and samples incubated at 37 °C for 30 min. Finally, gels were removed and placed in 10mL petri dishes filled with ddH2O for expansion. Water was exchanged at least twice every 30 min, and incubated in ddH2O overnight at RT. Gels expanded between 4× and 4.2× according to SA purity. Expanded cells were imaged with a UPlanS Apo 100×/1.4 oil immersion objective in an Olympus IX81 microscope (Olympus, Tokyo, Japan). For structured illumination microscopy (Sup Fig. 3A), a ZEISS Elyra 7 Lattice SIM was used.

Laser ablation (**Fig. 3I** and Sup. Fig. 3K-L) was performed at room temperature with a 100X oil Plan-Apochromat objective lens (NA 1.4) and an Axio-Observed.Z1 microscope (Carl Zeiss) equipped with a spinning disk confocal (Yokogawa), an EMCCD Evolve camera (Photometrics and Roper Scientific) and 491 nm (100 mW; Cobolt calypso) and 561 nm (100 mW; Cobolt Jive) lasers. Images were acquired with Metamorph software (Roper Scientific). Every 30 to 120 s, a Z-series of 0.4 µm steps were acquired. A 355 nm microchip laser (Teem Photonics) with a 21 kHz repetition rate, 0.8 µJ energy/pulse, 2 kW of peak power and 400 ps pulse width, powered with an iLas2 PULSE system (Roper Scientific) was used between 10 to 40 % power with one pulse of a spot length of 100 points. Breakage was considered as successful if a non-alignment between the two remaining Q-n MT bundle fragments was observed.

In **Fig.1H, F**; **Fig. 2B-C**; **Fig.3C**; **Fig. 4D, G**; Sup. Fig. 1I; Sup. Fig. 2E and Sup. Fig. 3A, a faint and fuzzy fluorescence signal was detected in some cell cytoplasm using the GFP filter set. This signal is not GFP but rather due to a non-specific yellow background fluorescence.

Z-stacks were deconvolved using the Deconvolution Lab plugin (**Fig. 1D, F**; **Fig. 3 C, E-F** **Fig. 4A, F**; Sup. Fig. 1E; Sup. Fig. 2A and Sup. Fig. 4B).

Image analysis

Distribution and associated statistics were performed using GraphPad Prism 5 (GraphPad Software, Inc. La Jolla, USA) and Excel (Microsoft). Unless specified, a student test (t-test with two independent samples) was used to compare two conditions. Among p-values obtained from biological repetitions in a same experiment (**Fig.1A**; **Fig. 2 B-C**; **Fig. 3D, F, H**; **Fig. 4 C, H**, and **Fig. 5C**), the indicated p-values are the highest measured among repeated experiments. P-values above 0.05 are indicated, while values below are depicted with ** ($0.05>p\text{-value}>1.10^{-4}$) and *** if p-value is less than 1.10^{-5} Histograms and scatter dot plots show the mean and the error bars indicate SD. MT length was measured on MAX-projected images using image-J.

For MT fluorescence intensity measurements (**Fig. 1B**, **Fig. 2D** and **Fig. 4D**) a line scan (i1) of 4 pixels width containing both FP signal and background was drawn along MTs on SUM projection images (4 z-plans) using ImageJ. A line of 8 pixels width (at the same location) was drawn in order to calculate the intensity of the surrounding background (i2). The real intensity (ir) was calculated as follow: $int = [i1 - ([(i2 \times i2_{surface}) - (i1 \times i1_{surface})] / (i2_{surface} - i1_{surface})) * i1_{surface}]$. We arbitrarily set the 'zero' at 0,5µm before the fluorescence increased onset on the SPB side in order to align all intensity measurements.

A similar approach was conducted to measure Tub4 fluorescence intensity (**Fig. 1E**, Sup. Fig. 1F) *i.e.* (i1) and (i2) were two boxes, the second including the first one. Intensity was calculated as follow: $int = [i1 - ([(i2 \times i2_{surface}) - (i1 \times i1_{surface})] / (i2_{surface} - i1_{surface})) * i1_{surface}]$.

For morphometric Q-nMT bundle property distribution (**Fig. 1C** and **4B**) the mean fluorescence intensity was measured in each individual cell, in a finite area localized adjacent to the SPB (0,4 µm – 3-4 Z stack sum projected) as an estimate of Q-nMT bundle width and plotted as a function of the according measured bundle length.

For Nuf2-GFP fluorescence intensity measurement at the SPB (Sup. Fig. 1E, bottom panel), GFP and RFP line scan measurements were done on a 4 Z-planes sum projection. The "SPB localization zone" was defined as the length ending 250 µm after the brightest RFP signal of Spc42-RFP. The remaining Q-nMT bundle zone was defined as the "+end zone". The total Nuf2-GFP signal detected along the Q-nMT bundle was set to 100 % to determine the percentage of the signal measured at the "SPB localization zone" and the "+end zone".

Normalized Q-nMT bundle length (**Fig. 3C**) was done after line scan intensity measurements. mTQZ-Tub1 intensity slopes were first aligned on their inflexion points. To compare Q-nMT bundles with different lengths, we first sorted Q-nMT bundles <1.8 µm. After an artificial isotropic expansion, we fit all MT structures to length order. Then, the corresponding mean intensity of the Q-nMT bundle (mTZQ-Tub1) and GFP signal were calculated.

To measure Q-nMT bundle depolymerization (**Fig. 5A** and Sup. Fig. 5B), individual Q-nMT bundle lengths were measured over time. The first length measurement was set to 100%. A fluorescence drop above or equal to 25 % defines the inflexion point of the slope, and was used to align the length measurements of different Q-nMT.

The FWHM (Full Width at Half Maximum, **Fig. 5B**) was calculated by measuring fluorescence intensity of a line crossing perpendicularly to a Q-nMT bundle at 0.5 µm from the SPB, using a sum projection. After fitting the intensity level with a Gaussian distribution and obtaining the standard deviation (σ) value, FWHM was calculated using the equation $2\sqrt{(2\ln 2)}x\sigma$.

Western blots

Western blots were done as described in (Sagot et al., 2006) using anti-GFP antibodies (Abcam); anti-Tat1 antibodies, a generous gift from J-P. Javerzat; antibody against the budding yeast Act1 or Sac6, generous gifts from B. Goode; and anti-TagRFP (mRuby2) antibodies, a generous gift from M. Rojo.

Phenotypical analysis of cells without Q-nMT bundle

WT strains were grown to glucose exhaustion (OD ~6.5, **Fig. 1F**) or to 5 d (Sup. Fig. 1L), washed-out with "old YPDA" (YPDA medium in which cells were grown for 4 d and then filtered to remove cells) pulsed with either DMSO alone or DMSO containing Noc (30 µg/mL final concentration) for 24 h. Cells were then washed twice in "old YPDA" before being incubated in the same medium. Dead cell measurement was done using methylene blue staining. The capacity of cells to exit quiescence (Sup. Fig. 1L, right panel) was scored after micro-manipulation of live cells (cells not stained with methylene blue) as described in (Laporte et al., 2011).

Supplemental data

Supplementary Figure 1 further describes the 3 steps of Q-nMT bundle formation. It shows the impact of physicochemical cell properties on MT stabilization and demonstrates that the Q-nMT bundle is required for both cell viability in quiescence and quiescence exit fitness.

Supplementary Figure 2 describes the impact of the alpha tubulin level on Q-nMT bundle assembly.

Supplementary Figure 3 demonstrates that kinetochore-MT interactions are not required for Q-nMT bundle maintenance and that mutants affected for kinetochore-kinetochore interactions have reduced viability in quiescence.

Supplementary Figure 4 further describes the impact of kinesin deletion on Q-nMT bundle morphometric parameters.

Supplementary Figure 5 explores Q-nMT bundle disassembly in mutants involved in mitotic spindle dismantlement.

Acknowledgements

The authors would like to thank the Bordeaux Imaging Center for the help in super-resolution imaging. We express our gratitude to E. O'Shea, A. Marston, S. Jaspersen, J-P. Javerzat, Wei-Lih Lee, C. Boone and B. Goode for sharing reagents and M. Rojo for providing us with the mCherry specific antibodies. We thank Michaël Gué (Zeiss) for helping us a with the lattice SIM Elyra 7 microscope. DL, AML, JD and IS were supported by a grant from the ANR-21-CE13-0023-01, La Ligue Contre le Cancer Régionale – Dordogne grant #193366 and the CNRS. MG and EN were supported by a National Science Foundation grant number MCB-1846262. AR was supported by the Conseil Régional d'Aquitaine (#20111301010) and the CNRS.

Author Contributions

D. Laporte did all the experiments described in this manuscript, except **Fig. 1F, 1H**, **Fig. 5 D-F**, Sup. 1H, Sup. 3E, J and Sup. Fig. 5I to K that were performed by A. Massoni-Laporte, together with all image deconvolution, and Sup. Fig. 2A and 3A that were done by J. Dompierre. A. Royou helped

for pulse-laser experiments of **Fig. 3I** and Sup Fig. 3K-L. C. Lefranc did molecular cloning and western blots. D. Mauboules performed yeast genetic for **Fig. 2**. M. L. Gupta Jr and E. T. Nsamba created the Tub1-only mutant (**Fig. 2**). L. Gal and M. Schuldiner performed high throughput deletion screen that originally uncovered mutants involved in Q-nMT bundle formation. IS and DL designed and supervised the experiments. IS and DL wrote the manuscript.

Abbreviations

- MT: microtubule
- SPB: spindle pole body
- GTP: guanosine triphosphate
- MTOC: microtubule organizing center
- ɣ-TuC: ɣ-tubulin complex
- MAPs: microtubule associated proteins
- Q-nMT bundle: quiescence specific nuclear microtubule bundle
- CPC: chromosome passenger complex

Supplementary Figure legends

Supplementary Figure 1

(A) Fluorescence intensity along MT structures in WT cells expressing mTQZ-Tub1. Mean intensity measurement for half pre-anaphase mitotic spindles (violet, n = 60), phase I (green, n = 19), and phase II (orange, n= 22) Q-nMT bundles. A line scan along the MT structure for an individual cell is shown as thin line, the mean as a bold line, all the lines being aligned at 0,5 µm before the fluorescence intensity increase onset on the SPB side.

(B) Individual Q-nMT bundle full width measured at half-maximum in WT cells (4 d) expressing mTQZ-Tub1 before or after 1 h after Noc treatment. A paired t-test was use to compare the two conditions (n > 40).

(C) Nuclear MT length in WT haploid (mat a and mat α) or diploid (mat a/mat α) cells expressing mTQZ-Tub1. Each circle represents an individual cell. Mean and SD are shown in red.

(D) Nuclear MT length in WT proliferating cells expressing mTQZ-Tub1 transferred to water, treated (+) or not (-) 15 min with 30 µg/ml Noc. Image of representative cells are shown, bar is 2 µm.

(E) WT cells expressing Spc42-RFP (red) and mTQZ-Tub1 (green, top panel) or Nuf2-GFP (green, bottom panel) upon entry into quiescence. The percentages indicate the relative amount of Nuf2-GFP detected at the SBP (blue arrowhead), bar is 1 µm.

(F) Tub4-mTQZ fluorescence intensity in WT cells of the W303 background. The mean and SD are shown; t-test was used to compare independent samples (N = 3, n > 150), ***: p-value < 1.10^{-5}.

(G) Fluorescence intensities in WT cells (4 d) expressing Tub4-mTQZ and mRuby-Tub1. The Tub4-mTQZ signal at the SBP is plotted as a function of the mRuby signal along the Q-nMT bundle. Each circle represents an individual cell (n = 60).

(H) Top panel: western blot using anti-GFP and anti-RFP antibodies on total protein extracts obtained from the indicated cells upon entry into quiescence. Anti-Ade13 antibodies are used as loading control. **Bottom panel**: images of representative WT cells expressing only pTUB1-mTQZ-

Tub1 (green) or only pADH2-mRuby-Tub1 (red) upon entry into quiescence as a control of cross channel fluorescence, bar is 2 µm.

(I) WT cells expressing mRuby-Tub1 (4 d) displaying both dynamic cMTs (red arrowhead) and a Q-nMT bundle (time is in min, bar is 1 µm).

(J) An artificial fluid phase to solid-like transition in proliferating cells does not induce MT stabilization. Proliferating WT cells expressing mTQZ-Tub1 (green) and Spc42-RFP (red) with fluid (pH = 7.5) or solid-like (pH = 4) cytoplasm/nucleoplasm (see materials and method) were incubated 15 min with 30 µg/ml Noc (left) or stained with phalloidin to detect actin (right). Indicated phenotypes were quantified (left and right graphs, N = 2, n > 115, mean and SD are indicated). Bar is 2 µm.

(K) Cells can assemble dynamic cMTs (red arrowhead) in quiescence. 2-day-old WT cells expressing mRuby-Tub1 were imaged after a 15 min Noc pulse-chase (30 µg/ml, time is in min). Red arrowhead: cytoplasmic MT, blue arrowhead: SBP, bar is 2 µm.

(L) Left graphs: WT cell viability after a 24h-pulse (grey rectangle) with Noc (30 µg/ml, circles) or DMSO (triangles), followed by a chase using carbon exhausted medium, the Noc pulse being done either upon glucose exhaustion or 5 days after glucose exhaustion. Each circle/triangle is the percentage obtained for an independent experiment in which n > 200 cells were scored. **Right graph:** live cells, as attested by a clear staining after a methylene blue treatment, were micro-separated 8 days after the Noc pulse done either upon glucose exhaustion or 5 d after glucose exhaustion, and allowed to give rise to a colony on a YPDA plate. Each circle/triangle is the percentage obtained for an independent experiment in which n > 100 cells were micro-separated. Images of representative YPDA plates after 3 d of growth at 30°C are shown. In E and K, blue arrowhead points to the SBP.

Supplementary Figure 2

(A) Expansion microscopy images of WT cells (4 d) expressing Tub3-3xGFP and immuno-stained with GFP (green) and α-tubulin (red) YOL1/2 antibodies, bar is 1 µm.

(B) Western blot using α-tubulin YOL1/2 antibody on total protein extracts from the indicated cells grown for 4 d. Actin was used as a loading reference. Numbers indicate the tubulin/actin ratio (mean for N = 8).

(C) Nuclear MT length in WT, *tub3Δ* and tub1-only cells expressing mTQZ-Tub1, 36 h (phase II, yellow) and 90 h (phase III, red) after glucose exhaustion, treated 15 min (blue) or not (grey) with 30 µg/ml Noc. Individual experiments from **Fig. 2B** and **Fig. 2C** are shown. P-values for Anova or unpaired t-test are indicated, ***: p-value < 1.10^{-5}.

(D) Nuclear MT length distribution in *yke2Δ*, *pac10Δ* or *gim3Δ* cells (4 d) and in corresponding WT cells expressing Nuf2-GFP (dark grey bars) or Bim1-3GFP (light grey bars). Right panel: western blot using an anti-α-tubulin antibody on total protein extracts from cells of the indicated genotype (4 d). Actin is a loading reference. The tubulin/actin ratio is indicated (N=4).

(E) Nuclear MT length distribution in *pac2Δ*, *cin2Δ* or *cin4Δ* (4 d) and in corresponding WT cells expressing Bim1-GFP (dark grey bars). Right panel: western blot using an anti-α-tubulin antibody on total protein extracts from cells of the indicated genotype (4 d). Actin is a loading reference. The tubulin/actin ratio is indicated (N=4).

Supplementary Figure 3

(A) Upper panel: WT cell (4 d) expressing Dad2-GFP and immuno-stained with GFP (green) and α-tubulin (red) YOL1/2 antibodies imaged using expansion microscopy. Blue is DAPI. **Lower panel:** WT cell (4 d) expressing Dad2-GFP (green) and mRuby-Tub1 (red), imaged using SIM. Bar is 1 µm.

(B) Nuclear MT length distribution in cells of the indicated genotypes, grown for 3 d at 25 °C, shifted to 37 °C or 25° C for 48 h, and treated 15 min or not with 30 µg/ml Noc. Each circle corresponds to the length of an individual MT structure, mean and SD are shown. ***: p-value < 1.10^{-6}. Images of representative cells are shown, bar is 2 µm.

(C) WT (grey) and *ipl1-1* cells (pink) expressing mTQZ-Tub1 were shifted upon glucose exhaustion to 37 °C for 48 h, and imaged after a 20 min Noc treatment (30 µg/ml). Same legend as in (B). Images of representative cells are shown, bar is 2 µm.

(D) Nuclear MT length in cells of the indicated genotypes, grown for 60 h in DMSO or 50 µM NA-PP1, treated 15 min or not with 30 µg/ml Noc. Same legend as in (B). Images of representative cells are shown, bar is 2 µm.

(E) Western blot using anti-myc antibodies on total protein extracts from *ipl1-5as*-myc cells treated 60 h with DMSO or 50 µM NA-PP1 after quiescence entry. Ade13 is the loading reference.

(F) Nuclear MT length in cells of the indicated genotypes grown 48 h at 37 °C or 96 h at 25 °C, treated 15 min or not with 30 µg/ml Noc. Same legend as in (B). Images of representative cells are shown, bar is 2 µm.

(G) Distribution of Bim1-3GFP intensity as a function of mTQZ-TUB1 intensity in individual Q-nMT bundles (green: phase I, 7 h after glucose exhaustion; orange, phase II, 26 h after glucose exhaustion and red, phase III, 50h after glucose exhaustion). Each circle represents an individual Q-nMT bundle.

(H) Viability (methylene blue staining) after the indicated time in quiescence (left graph), and capacity to form a colony after single live cell micro-manipulation after 12 days in quiescence (right graph). Pictures of representative plates 3 d after cell micro-manipulation are shown.

(I) Western blot using anti-GFP antibodies on total protein extracts from proliferating or 4-days-old cells expressing the indicated GFP fusion protein. Ade13 and Act1 are the loading controls.

(J) Percentage of cells of the indicated genotype displaying a MT star-like array. Each circle represents the % obtained for an independent culture (n > 200). Mean and SD are indicated.

(K) WT cells (6 d) expressing mRuby-Tub1 (red) and Nuf2-GFP (green) were transferred onto an agarose pad. Q-nMT bundles were cut using a pulsed laser (pink dashed line). White arrowheads point to dynamic cMTs. Time is in min, bar is 2 µm.

(L) Proliferating cells expressing mRuby-Tub1 (red) and Dad2-GFP (green) were transferred onto an agarose pad. Anaphase spindles were cut and the behavior of the released fragments was followed. Time is in min, bar is 2 µm.

(M) Nuclear MT length in cells of the indicated genotypes, grown for 3 d at 25 °C, shifted to 37 °C or 25° C for 48 h, and treated 15 min or not with 30 µg/ml Noc. Same legend as in (B). Images of representative cells are shown, p-value from unpaired t-test is indicated, bar is 2 µm.

Supplementary Figure 4

(A) Q-nMT bundle length as a function of Q-nMT bundle width for individual WT cells (grey) and *kar3Δ* cells (red) 90 h after glucose exhaustion.

(B) WT cells expressing mTQZ-Tub1 (red) and Cin8-GFP (green) were imaged at the indicated times after glucose exhaustion. Cells expressing only mTQZ-Tub1 (left panel) testify for the absence of fluorescence leak from the mTQZ signal into the GFP channel. Bar is 2µm.

(C) Fluorescence intensity along Q-nMT bundles in WT (black) and *cin8Δ* cells expressing mTQZ-Tub1, treated (green) or not (red) with Noc. Each line is an individual cell, the bold lines are the mean (n > 20).

(D) Morphometric Q-nMT bundle properties distribution in WT (grey) and *cin8Δ* (green) cells expressing mTQZ-Tub1. Each circle is an individual cell.

(E) Fluorescence intensity along Q-nMT bundles in WT (grey, n > 50), *kip1Δ* (red, n > 50), *bim1Δ* (green, n > 50), and *kip1Δ bim1Δ* (blue, n > 30) cells (4 d). Each line is an individual cell, the bold lines are the mean.

(F) Nuclear MT length distribution in *kip2Δ* cells expressing mTQZ-Tub1, treated 15 min (blue dots) or not (black dots) with 30 µg/ml Noc. For a comparison, the mean WT length is indicated as dashed line. Unpaired t-test p-values are indicated.

Supplementary Figure 5

(A) Representative 5-day-old cells (left and right) expressing mTQZ-Tub1 (red) and Nuf2-GFP (green) exiting quiescence on a YPDA agarose pad. Blue arrowhead: SBP; white arrows: Nuf2-GFP cluster. Time is in min, bar is 1µm.

(B). WT and *kip3Δ* cells (5 d) expressing Nuf2-GFP were re-fed on an YPDA microscope pad. Each line corresponds to an individual cell. Data were presented either (left) with the time set to zero at the onset MT depolymerisation or (right) at the onset of SPB separation (red dash line).

(C) Western blot using GFP antibodies on total protein extracts from WT cells expressing Kip3-GFP grown for the indicated time. Sac6 was used as a loading control.

(D-E) Nuclear Q-nMT bundle length in cells of the indicated genotype expressing mTQZ-Tub1, grown for 4 d and imaged at the indicated time after refeeding. For the rapamycin experiment in (D), WT cells were pre-incubated 1 h with rapamycin (1 µg/mL), and then re-fed in presence of the drug. For thermo-sensitive strains in (E), cells were grown 4 d at 25 °C, shifted 1 h at 37°C, and then transferred to new medium at 37 °C to trigger quiescence exit. Measurements were done after a 15 min Noc treatment (30 µg/ml) to remove dynamic cMTs. Each circle represents an individual cell. Mean and SD are indicated.

(F-G) Nuclear Q-nMT bundle length in cells of the indicated genotype expressing mTQZ-Tub1 were grown for the indicated time at 25 °C, shifted to 37 °C and re-fed. In G, measurements were done after a 15 min Noc treatment (30 µg/ml) to remove dynamic cMTs. Each circle represents an individual cell. Mean and SD are indicated.

(H) 3 individual experiments in which nuclear MT length was measured in 4-day-old *kip3Δshe1Δ* cells expressing mTQZ-Tub1 upon quiescence exit (n > 100). P-values from unpaired t-test are shown. Each circle represents an individual cell. Mean and SD are indicated.

(I) Percentage of cells with separated SPBs upon quiescence exit on YPDA agarose pad (N = 4, n > 200, left panel). Right: proliferation of WT and *kip3Δshe1Δ* strains in YPDA (OD 600nm as function of time).

(J) Q-nMT bundle length distribution in WT (grey) or *kip3Δshe1Δ* (green) cells with unseparated SPBs, 240 min after quiescence exit.

(K) Actin (red, phalloidin-staining) in WT and *kip3Δshe1Δ* cells expressing mTQZ-TUB1 (green) at the indicated time upon quiescence exit, bar is 2µm.

References

Acar S. *et al.* (2013) **The bipolar assembly domain of the mitotic motor kinesin-5** *Nat Commun* **4** https://doi.org/10.1038/ncomms2348

Aiken J., Moore J.K., Bates E.A. (2019) **TUBA1A mutations identified in lissencephaly patients dominantly disrupt neuronal migration and impair dynein activity** *Human Molecular Genetics* **28**:1227–1243 https://doi.org/10.1093/hmg/ddy416

Akhmanova A., Steinmetz M.O. (2015) **Control of microtubule organization and dynamics: two ends in the limelight** *Nature Reviews Molecular Cell Biology* **16**:711–726 https://doi.org/10.1038/nrm4084

Anvarian Z., Mykytyn K., Mukhopadhyay S., Pedersen L.B., Christensen S.T. (2019) **Cellular signalling by primary cilia in development, organ function and disease** *Nat Rev Nephrol* **15**:199–219 https://doi.org/10.1038/s41581-019-0116-9

Baas P.W., Rao A.N., Matamoros A.J., Leo L. (2016) **Stability properties of neuronal microtubules** *Cytoskeleton (Hoboken* **73**:442–460 https://doi.org/10.1002/cm.21286

Bahri H. *et al.* (2021) **TMEM70 forms oligomeric scaffolds within mitochondrial cristae promoting in situ assembly of mammalian ATP synthase proton channel** *Biochim Biophys Acta Mol Cell Res* **1868** https://doi.org/10.1016/j.bbamcr.2020.118942

Bergman Z.J., Xia X., Amaro I.A., Huffaker T.C. (2012) **Constitutive dynein activity in She1 mutants reveals differences in microtubule attachment at the yeast spindle pole body** *Mol Biol Cell* **23**:2319–2326 https://doi.org/10.1091/mbc.E12-03-0223

Bodakuntla S., Jijumon A.S., Villablanca C., Gonzalez-Billault C., Janke C. (2019) **Microtubule-Associated Proteins: Structuring the Cytoskeleton** *Trends Cell Biol* **29**:804–819 https://doi.org/10.1016/j.tcb.2019.07.004

Bode C.J., Gupta M.L., Suprenant K.A., Himes R.H. (2003) **The two alpha-tubulin isotypes in budding yeast have opposing effects on microtubule dynamics in vitro** *EMBO Rep* **4**:94–99 https://doi.org/10.1038/sj.embor.embor716

Bodrug T. *et al.* (2020) **The kinesin-5 tail domain directly modulates the mechanochemical cycle of the motor domain for anti-parallel microtubule sliding** *eLife* **9** https://doi.org/10.7554/eLife.51131

Burns S., Avena J.S., Unruh J.R., Yu Z., Smith S.E., Slaughter B.D., Winey M., Jaspersen S.L. (2015) **Structured illumination with particle averaging reveals novel roles for yeast centrosome components during duplication** *Elife* **4** https://doi.org/10.7554/eLife.08586

Cairo G., Lacefield S. (2020) **Establishing correct kinetochore-microtubule attachments in mitosis and meiosis** *Essays in Biochemistry* **64**:277–287 https://doi.org/10.1042/EBC20190072

Charruyer A., Ghadially R. (2018) **Influence of pH on Skin Stem Cells and Their Differentiation** *Curr Probl Dermatol* **54**:71–78 https://doi.org/10.1159/000489520

Cheeseman I.M., Chappie J.S., Wilson-Kubalek E.M., Desai A. (2006) **The conserved KMN network constitutes the core microtubule-binding site of the kinetochore** *Cell* **127**:983–997 https://doi.org/10.1016/j.cell.2006.09.039

Cleary J.M., Hancock W.O. (2021) **Molecular mechanisms underlying microtubule growth dynamics** *Curr Biol* **31**:R560–R573 https://doi.org/10.1016/j.cub.2021.02.035

Corbett K.D., Yip C.K., Ee L.-S., Walz T., Amon A., Harrison S.C. (2010) **The monopolin complex crosslinks kinetochore components to regulate chromosome-microtubule attachments** *Cell* **142**:556–567 https://doi.org/10.1016/j.cell.2010.07.017

Currie S.L., Xing W., Muhlrad D., Decker C.J., Parker R., Rosen M.K. (2023) **Quantitative reconstitution of yeast RNA processing bodies** *Proc Natl Acad Sci U S A* **120** https://doi.org/10.1073/pnas.2214064120

DeLuca K.F., Meppelink A., Broad A.J., Mick J.E., Peersen O.B., Pektas S., Lens S.M.A., DeLuca J.G. (2018) **Aurora A kinase phosphorylates Hec1 to regulate metaphase kinetochore-microtubule dynamics** *J Cell Biol* **217**:163–177 https://doi.org/10.1083/jcb.201707160

Dudziak A., Engelhard L., Bourque C., Klink B.U., Rombaut P., Kornakov N., Jänen K., Herzog F., Gatsogiannis C., Westermann S. (2021) **Phospho-regulated Bim1/EB1 interactions trigger Dam1c ring assembly at the budding yeast outer kinetochore** *EMBO J* **40** https://doi.org/10.15252/embj.2021108004

Dunn S., Morrison E.E., Liverpool T.B., Molina-París C., Cross R.A., Alonso M.C., Peckham M. (2008) **Differential trafficking of Kif5c on tyrosinated and detyrosinated microtubules in live cells** *J Cell Sci* **121**:1085–1095 https://doi.org/10.1242/jcs.026492

Fridman V., Gerson-Gurwitz A., Shapira O., Movshovich N., Lakämper S., Schmidt C.F., Gheber L. (2013) **Kinesin-5 Kip1 is a bi-directional motor that stabilizes microtubules and tracks their plus-ends in vivo** *J Cell Sci* **126**:4147–4159 https://doi.org/10.1242/jcs.125153

Fukuda Y., Luchniak A., Murphy E.R., Gupta M.L. (2014) **Spatial control of microtubule length and lifetime by opposing stabilizing and destabilizing functions of Kinesin-8** *Curr Biol* **24**:1826–1835 https://doi.org/10.1016/j.cub.2014.06.069

Goodson H.V., Jonasson E.M. (2018) **Microtubules and Microtubule-Associated Proteins** *Cold Spring Harb Perspect Biol* **10** https://doi.org/10.1101/cshperspect.a022608

Goto H., Inaba H., Inagaki M. (2017) **Mechanisms of ciliogenesis suppression in dividing cells** *Cell Mol Life Sci* **74**:881–890 https://doi.org/10.1007/s00018-016-2369-9

Gudimchuk N.B., McIntosh J.R. (2021) **Regulation of microtubule dynamics, mechanics and function through the growing tip** *Nat Rev Mol Cell Biol* **22**:777–795 https://doi.org/10.1038/s41580-021-00399-x

Guidi M., Ruault M., Marbouty M., Loïodice I., Cournac A., Billaudeau C., Hocher A., Mozziconacci J., Koszul R., Taddei A. (2015) **Spatial reorganization of telomeres in long-lived quiescent cells** *Genome Biol* **16** https://doi.org/10.1186/s13059-015-0766-2

Hahn I., Voelzmann A., Liew Y.-T., Costa-Gomes B., Prokop A. (2019) **The model of local axon homeostasis - explaining the role and regulation of microtubule bundles in axon maintenance and pathology** *Neural Dev* **14** https://doi.org/10.1186/s13064-019-0134-0

Heald R., Khodjakov A. (2015) **Thirty years of search and capture: The complex simplicity of mitotic spindle assembly** *J Cell Biol* **211**:1103–1111 https://doi.org/10.1083/jcb.201510015

Hibbel A., Bogdanova A., Mahamdeh M., Jannasch A., Storch M., Schäffer E., Liakopoulos D., Howard J. (2015) **Kinesin Kip2 enhances microtubule growth in vitro through length-dependent feedback on polymerization and catastrophe** *Elife* **4** https://doi.org/10.7554/eLife.10542

Huh W.-K., Falvo J.V., Gerke L.C., Carroll A.S., Howson R.W., Weissman J.S., O'Shea E.K. (2003) **Global analysis of protein localization in budding yeast** *Nature* **425**:686–691 https://doi.org/10.1038/nature02026

Jacquel B., Aspert T., Laporte D., Sagot I., Charvin G. (2021) **Monitoring single-cell dynamics of entry into quiescence during an unperturbed life cycle** *Elife* **10** https://doi.org/10.7554/eLife.73186

Janke C., Magiera M.M. (2020) **The tubulin code and its role in controlling microtubule properties and functions** *Nat Rev Mol Cell Biol* **21**:307–326 https://doi.org/10.1038/s41580-020-0214-3

Jin Q., Trelles-Sticken E., Scherthan H., Loidl J. (1998) **Yeast nuclei display prominent centromere clustering that is reduced in nondividing cells and in meiotic prophase** *J. Cell Biol* **141**:21–29

Joyner R.P., Tang J.H., Helenius J., Dultz E., Brune C., Holt L.J., Huet S., Müller D.J., Weis K. (2016) **A glucose-starvation response regulates the diffusion of macromolecules** *Elife* **5** https://doi.org/10.7554/eLife.09376

Kapitein L.C., Peterman E.J.G., Kwok B.H., Kim J.H., Kapoor T.M., Schmidt C.F. (2005) **The bipolar mitotic kinesin Eg5 moves on both microtubules that it crosslinks** *Nature* **435**:114–118 https://doi.org/10.1038/nature03503

Khodjakov A., La Terra S., Chang F. (2004) **Laser Microsurgery in Fission Yeast: Role of the Mitotic Spindle Midzone in Anaphase B** *Current Biology* **14**:1330–1340 https://doi.org/10.1016/j.cub.2004.07.028

Kim S., Tsiokas L. (2011) **Cilia and cell cycle re-entry: more than a coincidence** *Cell Cycle* **10**:2683–2690 https://doi.org/10.4161/cc.10.16.17009

Kirschner M., Mitchison T. (1986) **Beyond self-assembly: from microtubules to morphogenesis** *Cell* **45**:329–342

Kornakov N., Möllers B., Westermann S. (2020) **The EB1-Kinesin-14 complex is required for efficient metaphase spindle assembly and kinetochore bi-orientation** *J Cell Biol* **219** https://doi.org/10.1083/jcb.202003072

Laan L., Husson J., Munteanu E.L., Kerssemakers J.W.J., Dogterom M. (2008) **Force-generation and dynamic instability of microtubule bundles** *Proc Natl Acad Sci U S A* **105**:8920–8925 https://doi.org/10.1073/pnas.0710311105

Laporte D., Courtout F., Pinson B., Dompierre J., Salin B., Brocard L., Sagot I. (2015) **A stable microtubule array drives fission yeast polarity reestablishment upon quiescence exit** *J. Cell Biol* **210**:99–113 https://doi.org/10.1083/jcb.201502025

Laporte D., Courtout F., Salin B., Ceschin J., Sagot I. (2013) **An array of nuclear microtubules reorganizes the budding yeast nucleus during quiescence** *J. Cell Biol* **203**:585–594 https://doi.org/10.1083/jcb.201306075

Laporte D., Courtout F., Tollis S., Sagot I. (2016) **Quiescent Saccharomyces cerevisiae forms telomere hyperclusters at the nuclear membrane vicinity through a multifaceted mechanism involving Esc1, the Sir complex, and chromatin condensation** *Mol. Biol. Cell* **27**:1875–1884 https://doi.org/10.1091/mbc.E16-01-0069

Laporte D., Sagot I. (2014) **Microtubules move the nucleus to quiescence** *Nucleus* **5**:113–118 https://doi.org/10.4161/nucl.28538

Lee B.H., Kiburz B.M., Amon A. (2004) **Spo13 maintains centromeric cohesion and kinetochore coorientation during meiosis I** *Curr Biol* **14**:2168–2182 https://doi.org/10.1016/j.cub.2004.12.033

Liu P., Würtz M., Zupa E., Pfeffer S., Schiebel E. (2021) **Microtubule nucleation: The waltz between γ-tubulin ring complex and associated proteins** *Curr Opin Cell Biol* **68**:124–131 https://doi.org/10.1016/j.ceb.2020.10.004

Manning B.D., Barrett J.G., Wallace J.A., Granok H., Snyder M. (1999) **Differential regulation of the Kar3p kinesin-related protein by two associated proteins, Cik1p and Vik1p** *J Cell Biol* **144**:1219–1233 https://doi.org/10.1083/jcb.144.6.1219

Markus S.M., Omer S., Baranowski K., Lee W.-L. (2015) **Improved Plasmids for Fluorescent Protein Tagging of Microtubules in Saccharomyces cerevisiae** *Traffic* **16**:773–786 https://doi.org/10.1111/tra.12276

Meiring J.C.M., Shneyer B.I., Akhmanova A. (2020) **Generation and regulation of microtubule network asymmetry to drive cell polarity** *Curr Opin Cell Biol* **62**:86–95 https://doi.org/10.1016/j.ceb.2019.10.004

Mieck C., Molodtsov M.I., Drzewicka K., van der Vaart B., Litos G., Schmauss G., Vaziri A., Westermann S. (2015) **Non-catalytic motor domains enable processive movement and functional diversification of the kinesin-14 Kar3** *eLife* **4** https://doi.org/10.7554/eLife.04489

Mitchison T., Kirschner M. (1984) **Dynamic instability of microtubule growth** *Nature* **312**:237–242

Mittal P., Chavan A., Trakroo D., Shah S., Ghosh S.K. (2019) **Outer kinetochore protein Dam1 promotes centromere clustering in parallel with Slk19 in budding yeast** *Chromosoma* **128**:133–148 https://doi.org/10.1007/s00412-019-00694-9

Molines A.T. *et al.* (2022) **Physical properties of the cytoplasm modulate the rates of microtubule polymerization and depolymerization** *Developmental Cell* **57**:466–479 https://doi.org/10.1016/j.devcel.2022.02.001

Molodtsov M.I., Mieck C., Dobbelaere J., Dammermann A., Westermann S., Vaziri A. (2016) **A Force-Induced Directional Switch of a Molecular Motor Enables Parallel Microtubule Bundle Formation** *Cell* **167**:539–552 https://doi.org/10.1016/j.cell.2016.09.029

Movshovich N., Fridman V., Gerson-Gurwitz A., Shumacher I., Gertsberg I., Fich A., Hoyt M.A., Katz B., Gheber L. (2008) **Slk19-dependent mid-anaphase pause in kinesin-5-mutated cells** *J Cell Sci* **121**:2529–2539 https://doi.org/10.1242/jcs.022996

Munder M.C. *et al.* (2016) **A pH-driven transition of the cytoplasm from a fluid-to a solid-like state promotes entry into dormancy** *eLife* **5** https://doi.org/10.7554/eLife.09347

Muroyama A., Lechler T. (2017) **Microtubule organization, dynamics and functions in differentiated cells** *Development* **144**:3012–3021 https://doi.org/10.1242/dev.153171

Nsamba E.T., Bera A., Costanzo M., Boone C., Gupta Jr M.L. (2021) **Tubulin isotypes optimize distinct spindle positioning mechanisms during yeast mitosis** *Journal of Cell Biology* **220** https://doi.org/10.1083/jcb.202010155

Orij R., Postmus J., Ter Beek A., Brul S., Smits G.J. (2009) **In vivo measurement of cytosolic and mitochondrial pH using a pH-sensitive GFP derivative in Saccharomyces cerevisiae reveals a relation between intracellular pH and growth** *Microbiology* **155**:268–278 https://doi.org/10.1099/mic.0.022038-0

Pandey H., Popov M., Goldstein-Levitin A., Gheber L. (2021) **Mechanisms by Which Kinesin-5 Motors Perform Their Multiple Intracellular Functions** *Int J Mol Sci* **22** https://doi.org/10.3390/ijms22126420

Peris L., Wagenbach M., Lafanechère L., Brocard J., Moore A.T., Kozielski F., Job D., Wordeman L., Andrieux A. (2009) **Motor-dependent microtubule disassembly driven by tubulin tyrosination** *J Cell Biol* **185**:1159–1166 https://doi.org/10.1083/jcb.200902142

Persson L.B., Ambati V.S., Brandman O. (2020) **Cellular Control of Viscosity Counters Changes in Temperature and Energy Availability** *Cell* **183**:1572–1585 https://doi.org/10.1016/j.cell.2020.10.017

Peters L.Z., Hazan R., Breker M., Schuldiner M., Ben-Aroya S. (2013) **Formation and dissociation of proteasome storage granules are regulated by cytosolic pH** *J. Cell Biol* **201**:663–671 https://doi.org/10.1083/jcb.201211146

Petrovska I. *et al.* (2014) **Filament formation by metabolic enzymes is a specific adaptation to an advanced state of cellular starvation** *Elife* https://doi.org/10.7554/eLife.02409

Plowman R. *et al.* (2019) **The molecular basis of monopolin recruitment to the kinetochore** *Chromosoma* **128**:331–354 https://doi.org/10.1007/s00412-019-00700-0

Rabitsch K.P., Petronczki M., Javerzat J.P., Genier S., Chwalla B., Schleiffer A., Tanaka T.U., Nasmyth K. (2003) **Kinetochore recruitment of two nucleolar proteins is required for homolog segregation in meiosis I** *Dev Cell* **4**:535–548 https://doi.org/10.1016/s1534-5807(03)00086-8

Rabouille C., Alberti S. (2017) **Cell adaptation upon stress: the emerging role of membrane-less compartments** *Curr Opin Cell Biol* **47**:34–42 https://doi.org/10.1016/j.ceb.2017.02.006

Richmond D., Rizkallah R., Liang F., Hurt M.M., Wang Y. (2013) **Slk19 clusters kinetochores and facilitates chromosome bipolar attachment** *Mol Biol Cell* **24**:566–577 https://doi.org/10.1091/mbc.E12-07-0552

Roll-Mecak A (2020) **The Tubulin Code in Microtubule Dynamics and Information Encoding** *Dev Cell* **54**:7–20 https://doi.org/10.1016/j.devcel.2020.06.008

Roostalu J., Hentrich C., Bieling P., Telley I.A., Schiebel E., Surrey T. (2011) **Directional Switching of the Kinesin Cin8 Through Motor Coupling** *Science* https://doi.org/10.1126/science.1199945

Roostalu J., Surrey T. (2017) **Microtubule nucleation: beyond the template** *Nat. Rev. Mol. Cell Biol* https://doi.org/10.1038/nrm.2017.75

Röper K (2020) **Microtubules enter centre stage for morphogenesis** *Philos Trans R Soc Lond B Biol Sci* **375** https://doi.org/10.1098/rstb.2019.0557

Rutledge M.T., Russo M., Belton J.-M., Dekker J., Broach J.R. (2015) **The yeast genome undergoes significant topological reorganization in quiescence** *Nucleic Acids Res* **43**:8299–8313 https://doi.org/10.1093/nar/gkv723

Sagot I., Pinson B., Salin B., Daignan-Fornier B. (2006) **Actin bodies in yeast quiescent cells: an immediately available actin reserve?** *Mol. Biol. Cell* **17**:4645–4655 https://doi.org/10.1091/mbc.E06-04-0282

Sanchez A.D., Feldman J.L. (2017) **Microtubule-organizing centers: from the centrosome to non-centrosomal sites** *Curr. Opin. Cell Biol* **44**:93–101 https://doi.org/10.1016/j.ceb.2016.09.003

Schatz P.J., Solomon F., Botstein D. (1986) **Genetically essential and nonessential alpha-tubulin genes specify functionally interchangeable proteins** *Mol Cell Biol* **6**:3722–3733 https://doi.org/10.1128/mcb.6.11.3722-3733.1986

Scholey J.E., Nithianantham S., Scholey J.M., Al-Bassam J. (2014) **Structural basis for the assembly of the mitotic motor Kinesin-5 into bipolar tetramers** *Elife* **3** https://doi.org/10.7554/eLife.02217

Shapira O., Gheber L. (2016) **Motile properties of the bi-directional kinesin-5 Cin8 are affected by phosphorylation in its motor domain** *Sci Rep* **6** https://doi.org/10.1038/srep25597

Shimamoto Y., Forth S., Kapoor T.M. (2015) **Measuring Pushing and Braking Forces Generated by Ensembles of Kinesin-5 Crosslinking Two Microtubules** *Dev Cell* **34**:669–681 https://doi.org/10.1016/j.devcel.2015.08.017

Singh S.K., Pandey H., Al-Bassam J., Gheber L. (2018) **Bidirectional motility of kinesin-5 motor proteins: structural determinants, cumulative functions and physiological roles** *Cell. Mol. Life Sci* **75**:1757–1771 https://doi.org/10.1007/s00018-018-2754-7

Sirajuddin M., Rice L.M., Vale R.D. (2014) **Regulation of microtubule motors by tubulin isotypes and post-translational modifications** *Nat Cell Biol* **16**:335–344 https://doi.org/10.1038/ncb2920

Thawani A., Petry S. (2021) **Molecular insight into how γ-TuRC makes microtubules** *J Cell Sci* **134** https://doi.org/10.1242/jcs.245464

Thomas G.E. *et al.* (2016) **EB1 regulates attachment of Ska1 with microtubules by forming extended structures on the microtubule lattice** *Nat Commun* **7** https://doi.org/10.1038/ncomms11665

Tóth A., Rabitsch K.P., Gálová M., Schleiffer A., Buonomo S.B., Nasmyth K. (2000) **Functional genomics identifies monopolin: a kinetochore protein required for segregation of homologs during meiosis i** *Cell* **103**:1155–1168 https://doi.org/10.1016/s0092-8674(00)00217-8

Weinger J.S., Qiu M., Yang G., Kapoor T.M. (2011) **A nonmotor microtubule binding site in kinesin-5 is required for filament crosslinking and sliding** *Curr Biol* **21**:154–160 https://doi.org/10.1016/j.cub.2010.12.038

Wheway G., Nazlamova L., Hancock J.T. (2018) **Signaling through the Primary Cilium** *Frontiers in Cell and Developmental Biology* **6**

Wigge P.A., Jensen O.N., Holmes S., Souès S., Mann M., Kilmartin J.V. (1998) **Analysis of the Saccharomyces spindle pole by matrix-assisted laser desorption/ionization (MALDI) mass spectrometry** *J. Cell Biol* **141**:967–977

Winey M., Bloom K. (2012) **Mitotic spindle form and function** *Genetics* **190**:1197–1224 https://doi.org/10.1534/genetics.111.128710

Yukawa M., Teratani Y., Toda T. (2020) **How Essential Kinesin-5 Becomes Non-Essential in Fission Yeast: Force Balance and Microtubule Dynamics Matter** *Cells* **9** https://doi.org/10.3390/cells9051154

Zareiesfandabadi P., Elting M.W. (2022) **Force by minus-end motors Dhc1 and Klp2 collapses the S. pombe spindle after laser ablation** *Biophysical Journal* **121**:263–276 https://doi.org/10.1016/j.bpj.2021.12.019

Zeng X., Kahana J.A., Silver P.A., Morphew M.K., McIntosh J.R., Fitch I.T., Carbon J., Saunders W.S. (1999) **Slk19p is a centromere protein that functions to stabilize mitotic spindles** *J Cell Biol* **146**:415–425 https://doi.org/10.1083/jcb.146.2.415

Article and author information

Damien Laporte
Univ. Bordeaux, CNRS, IBGC, UMR 5095, Bordeaux, France
For correspondence: Damien.laporte@ibgc.cnrs.fr
ORCID iD: 0000-0002-1556-5253

Aurélie Massoni-Laporte
Univ. Bordeaux, CNRS, IBGC, UMR 5095, Bordeaux, France

Charles Lefranc
Univ. Bordeaux, CNRS, IBGC, UMR 5095, Bordeaux, France

Jim Dompierre
Univ. Bordeaux, CNRS, IBGC, UMR 5095, Bordeaux, France

David Mauboules
Univ. Bordeaux, CNRS, IBGC, UMR 5095, Bordeaux, France

Emmanuel. T. Nsamba
Genetics, Development, and Cell Biology, Iowa State University, Ames, IA 50011, USA

Anne Royou
Univ. Bordeaux, CNRS, IBGC, UMR 5095, Bordeaux, France

Lihi Gal
Department of Molecular Genetics, Weizmann Institute of Science, Rehovot, Israel

Maya Schuldiner
Department of Molecular Genetics, Weizmann Institute of Science, Rehovot, Israel
ORCID iD: 0000-0001-9947-115X

Mohan L. Gupta Jr
Genetics, Development, and Cell Biology, Iowa State University, Ames, IA 50011, USA

Isabelle Sagot
Univ. Bordeaux, CNRS, IBGC, UMR 5095, Bordeaux, France

Copyright

Editors

Reviewing Editor
Jens Lüders
Institute for Research in Biomedicine, Barcelona, Spain

Senior Editor
Benoît Kornmann
University of Oxford, Oxford, United Kingdom

Reviewer #1 (Public Review):

In their manuscript, Laporte et al. analyze the process of formation of the quiescent-cell nuclear microtubule (Q-nMT) bundle, a set of parallel MTs that emanate from the nuclear side of the spindle pole bodies (SPBs) upon the entry of Saccharomyces cerevisiae cells in quiescence. Based on their results, the authors propose that Q-nMT bundle formation is a multistep process that comprises three distinct sequential phases. The authors further evaluate the role of different factors during the growth of the Q-nMT bundle upon quiescence entry, as well as during the disassembly of this structure once the cells resume their proliferation.

The Q-nMT is an interesting cellular structure whose physiological function is still widely unknown. Hence, providing new insights into the dynamics of Q-nMT bundle formation and identifying new factors involved in this process is an interesting topic of relevance in the field. The authors made a substantial effort in order to evaluate Q-nMT bundle establishment and provide a considerable amount of data, mainly obtained from microscopy analyses.

Overall, the experiments are mostly well described and properly executed, and the data in the manuscript are clearly presented. Despite the interest of the study, nonetheless, there are several issues that could affect the validity of some conclusions drawn. In this way, regarding the analysis of the dynamics of Q-nMT bundle formation, the described experimental setup raises certain concerns, which mostly derive from the use of the microtubule-depolymerizing agent nocodazole as the only approach to evaluate this process. Also, regarding the factors involved in Q-nMT formation, the differences in microtubule length with the wild type strain, despite being statistically significant, are really subtle for many of the mutants analyzed (e.g., bir1, slk19, etc.). Furthermore, it is also puzzling that an effect on Q-nMT formation is proposed for meiosis-specific factors such as Mam1, which might as well be present during quiescence, but seems to be also detected in proliferating cells. Lastly, the evidence shown are insufficient to provide a direct link between defects in cell viability and aberrant Q-nMT formation.

https://doi.org/10.7554/eLife.89958.2.sa1

Reviewer #2 (Public Review):

Summary: The authors investigate the assembly of the Q-nMT, a stable microtubule structure that is assembled during quiescence. Notably, the authors show that the formation of the Q-nMT cannot be solely explained by changes in the physico-chemical properties of quiescent cells. The authors report that Q-nMT assembly occurs in three regulated steps and identify kinesin motor proteins involved in the assembly and disassembly of the structure.

Strengths: The findings provide new insight into the assembly and possible function of the Q-nMT with respect to the response of haploid budding yeast to glucose starvation.

Weaknesses: The manuscript would benefit from more precise language and requires additional clarification regarding how claims are supported by the evidence. Clear definitions are also required, for example "active process" is not defined. Some conclusions are not supported by the results, for example the claim that the Q-nMT functions as a checkpoint effector that inhibits re-entry into the cell cycle.

After reviewing the responses of the authors and the revised manuscript I am now satisfied with the study in its current form.

https://doi.org/10.7554/eLife.89958.2.sa0

Author Response

The following is the authors' response to the original reviews.

> ***Reviewer #1 (Recommendations for The Authors):***
>
> *To hopefully contribute to more strongly support the conclusions of the manuscript, I am including a series of concerns regarding the experiments, as well as some recommendations that could be followed to address these issues:*
>
> *(1) The Q-nMT bundle is largely unaffected by the nocodazole treatment in most phases during its formation. However, cells were only treated with nocodazole for a very short period of time (15 min). Have the authors analyzed Q-nMT stability after longer nocodazole exposures? Is a similar treatment enough to depolymerize the mitotic spindle? This result could be further substantiated by treatment with other MT-depolymerizing agents. Furthermore, the dynamicity of the Q-nMT bundle could be ideally also assessed by other techniques, such as FRAP.*

The experiments suggested by the reviewer have been published in our previous paper (Laporte et al, JCB 2013). In this previous study, we presented data demonstrating the resistance of the Q-nMT bundle to several MT poisons: TBZ, benomyl, MBC (Sup Fig 2D) and to an increasing amount of nocodazole after a 90 min treatment (Sup Fig2E). These published figures are provided below.

Author response image 1.

The nMT array contains highly stable MTS. (A) Variation Of nuclear MT length in function Of time (second) in proliferating cells. Cells express GFP•Tubl (green) and Nup2•RFP (red). Bars, 2 pm. N = l, n is indicated. (B) Variation of the nMT array length in function of time measured for BirnlGFP—expressing cells In = 161, for 6-d•old Dad2GFP—expressing cells In = 171, for Stu2GFP—expressing cells (n = 17), and 6•d-old Nuf2• GFP—expressing cells (n = 17). Examples Of corresponding time lapse are shown. Time is in minutes experiments). Bar, 2 pm. (CJ Nuf2•GFP dots detected along nMT array (arrow) are immobile. Several time lapse images of cells are shown. Time is in minutes. gar, 2 pm _ MT organizations in proliferating cells and 4-d•old quiescent cells before and after a 90-min treatment With indicated drugs. Bar, 2 pm. (E) MT organizations in Sci-old quiescent cells before and after a 90min treatment With increasing concentrations Of nocodazole.

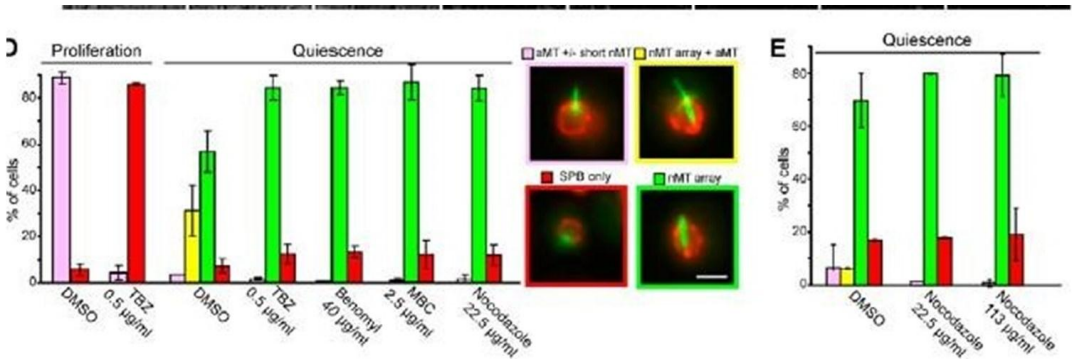

In the same article, we showed that Q-nMT bundles resist a 3h nocodazole treatment, while all MT structures assembled in proliferating cells, including mitotic spindle, vanished (see Fig 2E below). In addition, in our previous article, FRAP experiments were provided in Fig 2D.

Author response image 2.

The nuclear array is composed of stable MTS. Variation of the length in function of time of (A) aMTs in proliferating cells, (B) nMT array in quiescent cells (7 d), and the two MT structures in early quiescent cells (4 d). White arrows point ot dynamic aMTs. In A—C, N = 2, n is indicated ID) FRAP on 7-d-old quiescent cells. White arrows point to bleach areas. Error bars are SEM. In A—D. time is in seconds. (E) nMT array is not affected by nocodazole treatment. Before and various times after carbon exhaustion (red dashed line), cells were incubated for 3 h with 22.5 pg/pL nocodozole and then imaged. The corresponding control experiment is shown in Fig I A. In all panels, cells expressing GFP-TtJbl (green) and Nup2-RFP (red) are shown; bars, 2 pm.

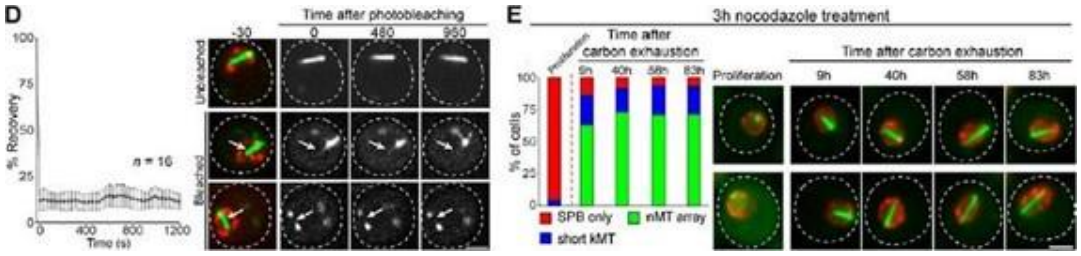

This previous study was mentioned in the introduction and is now re-cited at the beginning of the results section (line 107-108).

As expected from our previous study, when proliferating cells were treated with Noc (30 µg/ml) in the same conditions as in Fig1, most of the short and the long mitotic spindles vanished after a 15 min treatment as shown in the graph below.

Author response image 3.

Proliferating cells expressing NOf2=GFP and mTQZ-TUb1 (00—2) were treated or not With NOC (30vgfmI) for 15 min.% Of cells With detectable MT and representative cells are shown. Khi-teet values are indicated. Bar: 2 pm,

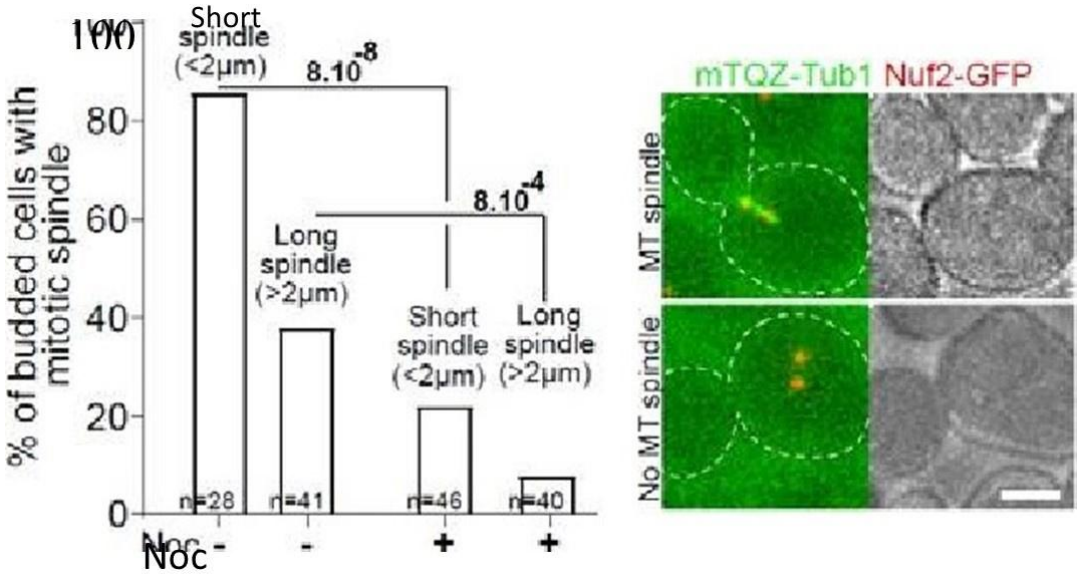

> *(2) The graph in Figure 1B is somewhat confusing. Is the X-axis really displaying the length of the MTs as stated in the legend? If so, one would expect to see a displacement of the average MT length of the population as cells progress from phase II to phase III, as previously demonstrated in Figure 1A. Likewise, no data points would be anticipated for those phases in which the MT length is 0 or close to 0. Moreover, when the length of half pre-anaphase mitotic spindle was measured as a control, how can one get MT lengths that are equal or close to 0 in these cells? The length of the pre-anaphase spindle is between 2-4 um, so MT length values should range from 1 to 2 um if half the spindle is measured.*

The graph in Fig1B represents the fluorescence intensity (a proxy for the Q-nMT bundle thickness) along the Q-nMT bundle length.

Fluorescence intensity is measured along a “virtual line” that starts 0,5 µm before the extremity of the QnMT bundle that is in contact with the SPB. In other words, we aligned all intensity measurements at the fluorescence increasing onset on the SPB side. We arbitrarily set the ‘zero’ at 0,5um before the fluorescence increased onset. That is why the fluorescence intensity is zero between 0 and 0,5 µm – The X-axis represents this virtual line, the 0 being set 0,5 µm before the Q-nMT bundle extremity on the SPB side. This virtual line allows us to standardize our “thickness” measurements for all Q-nMT bundles.

Using this standardization, it is clear that the length of the Q-nMT bundles increased from phase II to III (see the red arrow). Yet, as in phase II, Q-nMT bundles are not yet stable, their lengths are shorter in phase II than in phase II after a Noc treatment (compare the end of the orange line and the end of the blue line in phase II).

Author response image 4.

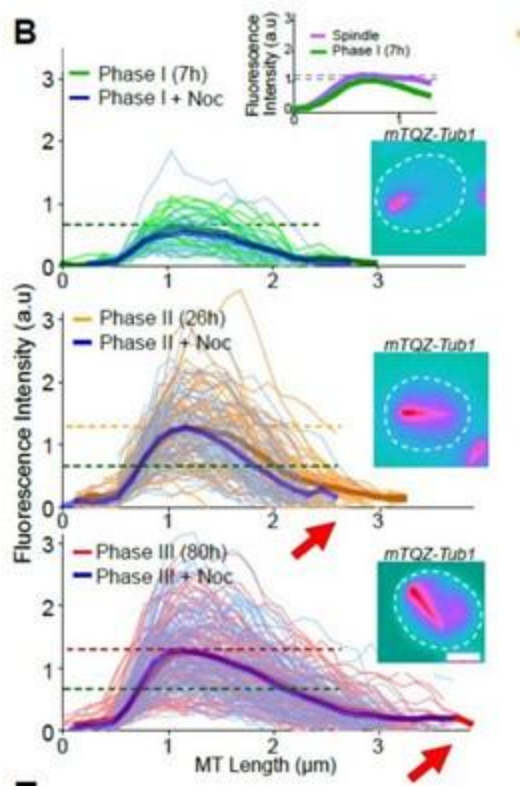

This is now explained in details in the Material and Methods section (line 539-545).

This is the same for the inset of Fig 1B and in Sup Fig 1A, in which we measured fluorescence intensity along the halfmitotic spindle just as we did for MT bundle. The X-axis represent a virtual line along the mitotic spindle, starting 0,5 µm before the SBP spindle extremity.

Author response image 5.

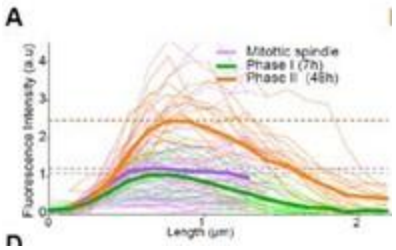

> *(3) Microtubules seem to locate next to or to extend beyond the nucleus in the control cells (DMSO) in Figure 1H. Since both nuclear MTs and cytoplasmic MTs emanate from the SPBs, it would have been desirable to display the morphology of the nucleus when possible. Moreover, since the nucleus is a tridimensional structure, it would also be advisable to image different Z-sections.*

Analysis demonstrating that Q-nMT bundles are located inside the nucleus have been provided in our previous paper (Laporte et al, JCB 2013). In this article most of the images are maximal projections of Z-stacks in which the nuclear envelope is visualized via Nup2-RFP (see Fig1 of Laporte et al, JCB 2013 as an example below).

Author response image 6.

MTsare organized as a nuclear array in quiescent cells. (A) MT reorganization upon quiescence entry. Cells expressing GFP-Tub1 (green) and Nup2RFP (red) are shown. Glucose exhaustion is indicated as a red dashed line. Quiescent cells dl expressing Tub I-RFP and either Spc72GFP,

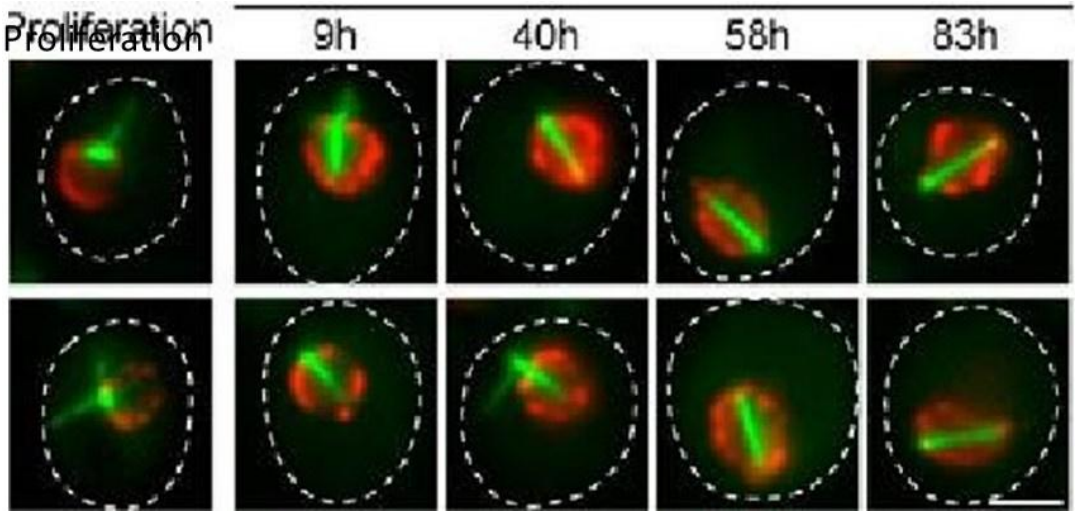

In Laporte et al, JCB 2013, we also provided EM analysis both in cryo and immune-gold (Fig 1E below).

Author response image 7.

(top) or coexpr;sse8 with Tub I-RFP (bottom). Arrows point dot along the nMT array. Bars: (A —C)) 2 pm. (E) AMT arroy visualized in WT cells by EMI Yellow arrows, MTS; red arrowheads,

nuclear membrane; pink arrow, SPB. Insets: nMT cut transversally. Bar, 100 nm.

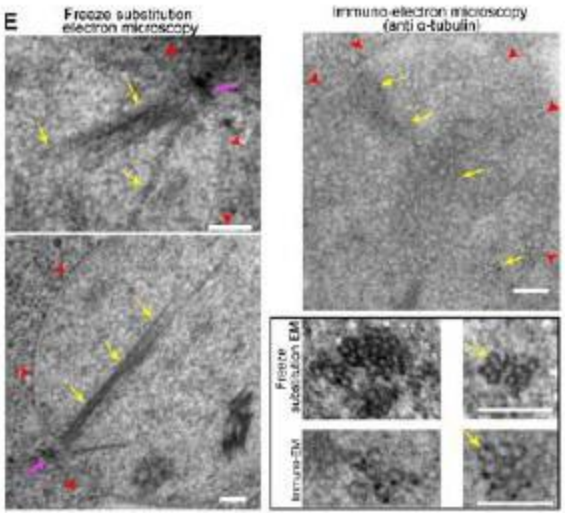

> *(4) Movies depicting the process of Q-nMT bundle formation in live cells would have been really informative to more precisely evaluate the MT dynamics. Likewise, together with still images (Fig 1D and Supp. Fig. 1D), movies depicting the changes in the localization of Nuf2-GFP would have further facilitated the analysis of this process.*

In a new Sup Fig 1E, we now provide images of Q-nMT bundle formation initiation in phase I, in which it can be observed that Nuf2-GFP accompanies the growth of MT (mTQZ-TUB1) at the onset of Q-nMT bundle formation. Unfortunately, it is technically very challenging to follow the entire process of Q-nMT bundle formation in individual cells, as it takes > 48h. Indeed, for movies longer than 24h, on both microscope pads or specific microfluidic devices (Jacquel, et al, eLife 2021), phototoxicity and oxygen availability become problematic and affect cells' viability.

> *(5) Western blot images displaying the relative protein levels for mTQZ-Tub1 and of the ADH2 promoter-driven mRuby-Tub1 at the different time points should be included to more strongly support the conclusion that new tubulin molecules are introduced in the Q-nMT bundle only after phase I. It is worth noting, in this sense, that the percentage of cells with 2 colors Q-nMT bundle is analyzed only 1 hour after expression of mRuby-Tub1 was induced for phase I cells, but after 24 hours for phase II cells.*
> *We have modified Fig 1F and now provide images of cells after 3, 6 and 24h after glucose exhaustion and the corresponding percentage of cells displaying Q-nMT bundle with the two colors. We also now provide a western blot in Sup Fig 1H using specific antibodies against mTQZ (anti-GFP) and mRuby (anti-RFP).*
>
> *(6) In order to demonstrate that Q-nMT formation is an active process induced by a transient signal and that the Q-nMT bundle is required for cell survival, the authors treated cells with nocodazole for 24 h (Fig 1H and Supp Fig 1K). Both events, however, could be associated with the toxic effects of the extremely prolonged nocodazole treatment leading to cell death.*

We have treated 5 days old cells for 24h with 30 µg/ml Noc. We then washed the drug and transferred the cells into a glucose free medium. We then followed both cell survival, using methylene blue, and the cell's capacity to form a colony after refeeding. In these conditions,

we did not observe any toxic effect of the nocodazole. This result is now provided in Sup Fig 1L and discussed line 172-176.

> *(7) The "Tub1-only" mutant displays shorter but stable Q-nMT bundles in phase II, although they are thinner than in wild-type cells. What happens in the "Tub3-only" mutant, which also has beta-tubulin levels similar to wild-type cells (Supp. Fig. 2B)?*

In order to measure Q-nMT bundle length and thickness, we used Tub1 fused to GFP. This cannot be done in a Tub3-only mutant. Yet, we have measured Q-nMT bundle length in Tub3-only cells using Bim1-3GFP as a MT marker (as in Laporte et al, JCB 2013). As shown in the figure below, Q-nMT bundles were shorter in Tub3-only cells than in WT cells whatever the phase.

Author response image 8.

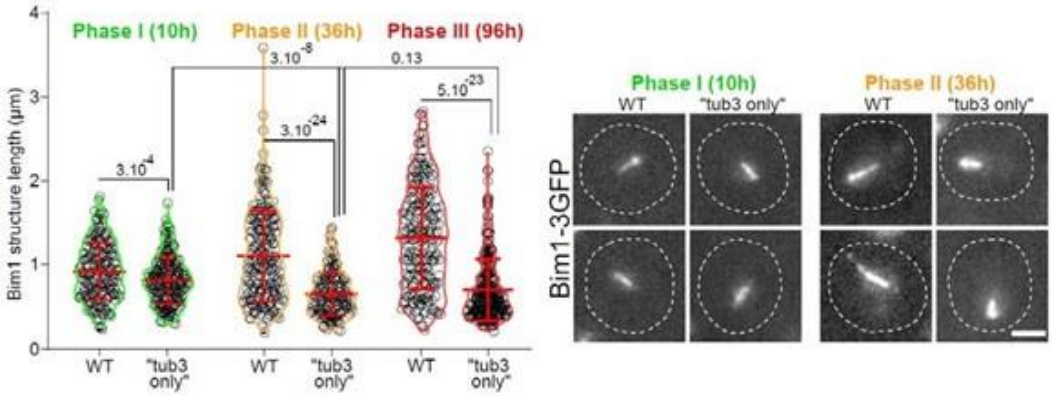

We do not know if this effect is directly linked to the absence of Tub1 or if it is very indirect and for example due to the fact that Tub1 and Tub3 interact differently with Bim1 or other proteins that are involved in Q-nMT bundle stabilization. As we cannot give a clear interpretation for that result, we decided not to present those data in our manuscript.

> *(8) Why were wild-type and ndc80-1 cells imaged after a 20 min nocodazole treatment to evaluate the role of KT-MT attachments in Q-nMT bundle formation (Fig 3A)? Importantly, this experiment is also missing a control in which Q-nMT length is analyzed in both wild-type and ndc80-1 cells at 25ºC instead of 37ºC.*

In this experiment, we used nocodazole to test both the formation and the stability of the Q-nMT bundle. Fig 3A shows MT length distribution in WT (grey) and ndc80-1 (violet) cells expressing mTQZTub1 (green) and Nuf2-GFP (red), shifted to 37 °C at the onset of glucose exhaustion and kept at this non-permissive temperature for 12 or 96 h then treated with Noc. The control experiment was provided in Sup Fig 3B. Indeed, this figure shows MT length in WT (grey) and ndc80-1 (violet) expressing mTQZ-Tub1 (green) and Nuf2-GFP (red) grown for 4 d (96h) at 25 °C, and treated or not with Noc. This is now indicated in the text line 216 and in the figure legend line 976

Author response image 9.

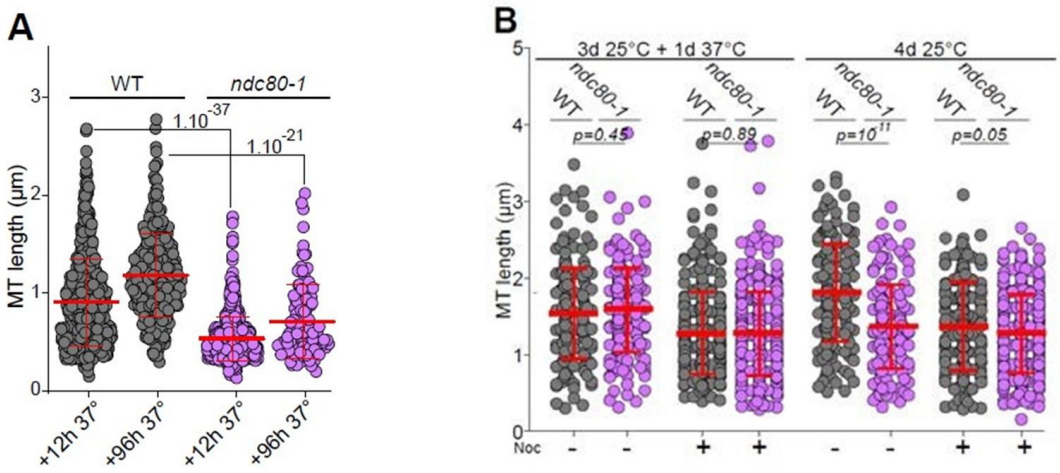

> *(9) As a general comment linked to the previous concern, it is striking that in many instances, Q-nMT bundle length is measured after nocodazole treatment without any evident reason to do this and without displaying the results in untreated cells as a control. If nocodazole is used, the authors should explicitly indicate it and state the reason for it.*

We provide control experiments without nocodazole for all of the figures. For the sake of figure clarity, for Fig.3A the control without the drug is in Sup. Fig. 3B, for Fig. 3B it is shown in Sup. Fig. 3D, for Fig. 4B, it is shown in Sup. Fig 4A. This is now stated in the text and in the figure legend: for Fig. 3A: line 216 and in the figure legend line 976; for Fig. 3B: line 222 and figure legend line 984; for Fig. 4B: line 280 and in the figure legend line 1017.

The only figures where the untreated cells are not shown is for Fig 1D since the goal of the experiment is to make dynamic MTs shorten.

In Fig. 5C and Sup. Fig. 5D to F, we used nocodazole to get rid of dynamic cytoplasmic MTs that form upon quiescence exit in order to facilitate Q-nMT bundle measurement. This was explained in our previous study (Laporte et al, JCB 2013). We now mention it in the figure legends, see for example Fig. 5 legend line 1054.

> *(10) Ipl1 inactivation using the ipl1-1 thermosensitive allele impedes Q-nMT bundle formation. The inhibitor-sensitive ipl1-as1 allele could have been further used to show whether this depends on its kinase activity, also avoiding the need to increase the temperature, which affects MT dynamics. As suggested, we have used the ipl1-5as allele. We have thus modified Fig 3B and now show that is it indeed the Ipl1 kinase activity that is required for Q-nMT bundle formation initiation (line 222). In any case, it is surprising that deletion of SLI15 does not affect Q-nMT formation (in fact, MT length is even larger), despite the fact that Sli15, which localizes and activates Ipl1, is present at the Q-nMT (Fig 3C). Likewise, deletion of BIR1 has barely any effect on MT length after 4 days in quiescence (Fig 3D). Do the previous observations mean that Ipl1 role is CPC-independent? Does the lack of Sli15 or Bir1 aggravate the defect in Q-nMT formation of ipl1-1 cells at non-permissive or semi-permissive temperature?*

Thanks to the Reviewer's comments, we have re-checked our sli15Δ strain and found that it was accumulating suppressors very rapidly. To circumvent this problem, we utilized the previously described sli15-3 strain (Kim et al, JCB 1999). We found that sli15-3 was synthetic

lethal with both ipl1-1, ipl1-2 (as described in Kim et al, JCB 1999) and with ipl1-as5, preventing us from addressing the CPC dependence of the Ipl1 effect asked by the Reviewer. However, using the sli15-3 strain, we now show that inactivation of Sli15 upon glucose exhaustion does prevent Q-nMT bundle formation (See new Sup Fig 3F and the text line 226-227).

> *(11) Lack of both Bir1 and Bim1 act in a synergistic way with regard to the defect in Q-nMT bundle formation. Although the absence of both Sli15 and Bim1 is proposed to lead to a similar defect, this is not sustained by the data provided, particularly in the absence of nocodazole treatment (Supp. Fig 3E).*

Deletion of bir1 alone has only a subtle effect on Q-nMT bundle length in the absence of Noc, yet in bir1Δ cells, Q-nMT bundles are sensitive to Noc. Deletion of BIM1 (bim1Δ) aggravates this phenotype (Fig. 3D). As mentioned above, Q-nMT bundle formation is impaired in sli15-3 cells. In our hands, and as expected from (Zimnaik et al, Cur Biol 2012), this allele is synthetic lethal with bim1Δ.

> *On the other hand, the simultaneous lack of Bir1 and Bim1 drastically reduces the viability of cells in quiescence and this is proposed to be evidence supporting that KT-MT attachments are critical for QnMT bundle assembly (Supp Fig 3G). However, similarly to what was indicated previously for the 24 h nocodazole treatment, here again, the lack of viability could be originated by other reasons that are associated with the lack of Bir1 and Bim1 and not necessarily with problems in Q-nMT formation. In fact, the viability defect of cells lacking Bir1 and Bim1 is similar to that of cells only lacking Bir1 (Supp Fig 3G).*

We have previously shown that many mutants impaired for Q-nMT bundle formation (dyn1Δ, nip100Δ etc) have a reduced viability in quiescence (Laporte et al, JCB 2013). In the current study, a very strong phenotype is observed for other mutants impaired for Q-nMT bundle formation such as bim1Δ bir1Δ cells, but also for slk19Δ bim1Δ.

Importantly, as shown in the new Sup Fig 1L, in WT cells treated with Noc upon entry into quiescence, a treatment that prevents Q-nMT formation, showed a reduced viability, while a Noc treatment that does not affect Q-nMT bundle formation, i.e. a treatment in late quiescence, has no effect on cell survival. This solid set of data point to a clear correlation between the ability of cells to assemble a Q-nMT bundle and their ability to survive in quiescence. Yet, of course, we cannot formally exclude that in all these mutants, the reduction of cell viability in quiescence is due to another reason.

> *(12) Both Mam1 and Spo13 are, to my knowledge, meiosis-specific proteins. It is therefore surprising that mutants in these proteins have an effect on MT bundle formation (Fig 3G-H, Supp. Fig. 3G). Are Mam1 and Spo13 also expressed during quiescence? Transcription of MAM1 or SPO13 does not seem to be induced by glucose depletion in previously published microarray experiments, but if Mam1 are Spo13 are expressed in quiescent cells, the authors should show this together with their results. Indeed, it is interesting to notice that Mam1 and Spo13 are involved in both meiosis and Q-nMT bundle formation. As suggested by the Reviewer we have performed western blots in order to address the expression of those proteins in proliferation and quiescence (4d). We tagged Spo13 with either GFP, HA or Myc but none of the fusion proteins were functional. Yet, as shown in the new Sup Fig 3I, Mam1-GFP, Csm1-GFP and Lsr4-GFP were expressed both in proliferation and quiescence.*
>
> *(13) In the laser ablation experiments that demonstrate that KT-MT attachments are not needed in order to maintain Q-nMT bundles once formed, anaphase spindles of proliferating cells were cut as a control (Supp. Fig 3I). However, late anaphase cells have*

> *already segregated the chromosomes, which lie next to the SPBs (this can be evidenced by looking at Dad2-GFP localization in Supp. Fig 3I), so that only interpolar MTs are severed in these experiments. The authors should have instead used metaphase cells as a control, since chromosomes are maintained at the spindle midzone and the length and width of the metaphase spindle is more similar to that of the Q-nMT bundle.*

We have tried to "cut" short metaphase spindles, but as they are < 1 µm, after the laser pulse, it is difficult to verify that spindles are indeed cut and not solely "bleached". Furthermore, after the cut, the remaining MT structure that is detectable is very short, and we are not confident in our length measurements. Yet, this type of experiment has been done in S. pombe (Khodjakov et al, Cur Biol 2004 and Zareiesfandabadi et al, Biophys. J. 2022). In these articles the authors have demonstrated that after a cut, metaphase spindles are unstable and rapidly shrink through the action of Kinesin14 and dynein. This is now mentioned in the text line 265.

> *(14) In the experiment that shows that cycloheximide prevents Q-nMT disassembly after quiescence exit, and therefore that this process requires de novo protein synthesis (Fig. 5A), cells are indicated to express only Spc42-RFP and Nuf2-GFP. However, Stu2-GFP images are also shown next to the graph and, according to the figure legend, it was indeed Stu2-GFP that was used to measure individual QnMT bundles in cells treated with cycloheximide. In the graph, additionally, time t=0 represents the onset of MT bundle depolymerization, but Q-nMT bundle disassembly does not take place after cycloheximide treatment. The authors should clarify these aspects of the experiment.*

Following the Reviewer's suggestion, to clarify these aspects we have split Fig. 5A into 2 panels.

> *Finally, some minor issues are:*
>
> *(1) The text should be checked for proper spelling and grammar.*

We have done our best.

> *(2) In some instances, there is no indication of how many cells were imaged and analyzed.*

We now provide all these details either in the figure itself or in the figure legend.

> *(3) Besides the Q-nMT bundle, it is sometimes noticeable an additional strong cytoplasmic fluorescent signal in cells that express mTQZ-Tub1 and/or mRuby-Tub1 (e.g., Figs 1F, 1H and, particularly, Supp Fig 1H). What is the nature of these cytoplasmic MT structures?*

We did mention this observation in the material and methods section (see line 526-528). This signal is a background fluorescence signal detected with our long pass GFP filter. It is not GFP as it is "yellowish" when we view it via the microscope oculars. This background signal can also be observed in quiescent WT cells that do not express any GFP. We do not know what molecule could be at the origin of that signal but it may be derivative of an adenylic metabolite that accumulates in quiescence and could be fluorescent in the 550nm –ish wavelength, but this is pure speculation.

> *(4) It is remarkable that a 20-30% decrease in tubulin levels had such a strong impact on the assembly of the Q-nMT bundle (Supp. Fig. 2). Can this phenotype be recovered by increasing the amount of tubulin in the mutants impaired for tubulin folding?*

Yes, this is astonishing, but we believe our data are very solid since we observed that with both tub3Δ and in all the tubulin folding mutants we have tested (See Sup. Fig. 2). To answer Reviewer's question, we would need to increase the amount of properly folded tubulin, in a tubulin folding mutant. One way to try to do that would be to find suppressors of GIM mutations, but this is a lengthy process that we feel would not add much strength to this conclusion.

> *(5) The graphs displaying the length of the Q-nMT bundle in several mutants in microtubule motors throughout a time course are presented in a different manner than in previous experiments, with data points for individual cells being only shown for the most extreme values (Fig 4C, 4H). It would be advisable, for the sake of comparison, to unify the way to represent the data.*

We have now unified the way we present our figures.

> *(6) How was the exit from quiescence established in the experiments evaluating Q-nMT disassembly? How synchronous is quiescence exit in the whole population of cells once they are transferred to a rich medium?*

We set the "zero" time upon cell refeeding with new medium. In fact, quiescence exit is NOT synchronous. We have reported this in previous publications, with the best description of this phenomena being in Laporte et al, MIC 2017 .
The figures below are the same data but on the left graph, the kinetic is aligned upon SPB separation onset, while on the right graph (Fig 5A), it is aligned on MT shrinking onset.

Author response image 10.

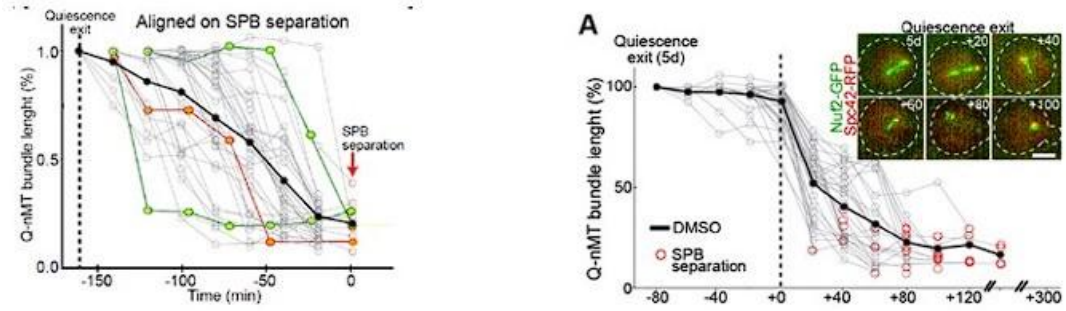

We can add this piece of data in a Sup Figure if the Reviewer believes it is important.

> ***Reviewer #2 (Recommendations For The Authors):***
>
> *General:*
>
> - *In general, more precise language that accurately describes the experiments would improve the text.*
>   *We have tried to do our best to improve the text.*
> - *The authors should clearly define what they mean by an active process and provide context to support this statement regarding the Q-nMT.*

We have strived to clarify this point in the text (see paragraph form line 146 to 178).

- *It is reasonable to assume that structures composed of microtubules are dynamic during the assembly process. The authors should clarify what they mean by "stable by default i.e., intrinsically stable." Do they mean that when Q-nMT assembly starts, it will proceed to completion regardless of a change in condition?*

We mean that in phase I the Q-nMT bundle is stabilized as it grows and that stabilization is concomitant with polymerization. By contrast, MTs polymerized during phase II are not stabilized upon elongation beyond the phase I polymer, and get stabilized later, in a separate phase (i.e. in phase III). We hope to have clarified this point in the text (see line 108-110).

- *In lines 33-34, the authors claim that the Q-nMT bundle functions as a "sort of checkpoint for cell cycle resumption." This wording is imprecise, and more significantly the authors do not provide evidence supporting a direct role for Q-nMT in a quiescence checkpoint that inhibits re-entry into the cell cycle.*

We have softened and clarified the text in the abstract (see line 29-30)., in the introduction (line 101104), in the result section (line 331-332) and in the discussion (line 426-430).

- *Many statements are qualitative and subjective. Quantitative statements supported by the results should be used where possible, and if not possible restated or removed.*

We provide statistical data analysis for all the figures.

- *The number of hours after glucose exhaustion used for each phase varies between assays. This is likely a logistical issue but should be explained.*

This is indeed a logistical issue and when pertinent, it is explained in the text.

- *It would be interesting to address how this process occurs in diploids. Do they form a Q-nMT? How does this relate to the decision to enter meiosis?*

Diploid cells enter meiosis when they are starved for nitrogen. Upon glucose exhaustion diploids do form a Q-nMT bundle. This is shown and measured in the new Sup Fig1C. In fact, in diploids, Q-nMT bundles are thicker than in haploid cells.

- *It would be interesting to address how the timescale of this process compares to the types of nutrient stress yeast would be exposed to in the environment.*

We have transferred proliferating yeast cells to water, to try to mimic what could happen when yeast cells face rain in the wild. As shown below, they do form a Q-nMT bundle that becomes nocodazole resistant after 30h. This data is now provided in the new Sup Fig 1D.

- *It is recommended that the authors use FRAP experiments to directly measure the stability of the QnMT bundles.*

This experiment was published in (Laporte et al, 2013). Please see response to Reviewer #1.

- *In many cases, the description of the experimental methods lacks sufficient detail to evaluate the approach or for independent verification of results.*

We have strived to provide a more detailed material and methods section, as well as more detailed figure legends and statistical informations.

> *Specific comments on figures:*
>
> - *In Figure 1 c), what do the polygons represent? They do not contain all the points of the associated colour.*

The polygon represented the area of distribution of 90% of the data points. As they did not significantly add to the data presentation they have been removed.

> - *In Figure 2 a), is the use of two different sets of markers to control for the effect of the markers on microtubule dynamics?*

Yes, we are always concerned about the influence of GFP on our results, so very often we replicate our experiments with different fluorescent proteins or even with different proteins tagged with GFP. This is now mentioned in the text (line 184-186).

> - *Is it accurate to say (line 201, figure 3 a)) that no Q-nMT bundles were detected in ndc80-1 cells shifted to 37 degrees, or are they just shorter?*

As shown in Fig 3A, in ndc80-1 cells, most of the MT structures that we measured are below 0,5um. This has been re-phrased in the text (line 214-215).

> - *Lines 265-269, figure 4 b), how can the phenotype observed in cin8Δ cells be explained given the low abundance of Cin8 that is detected in quiescent cells?*

Faint fluorescence signal is not synonymous of an absence of function. As shown in Sup Fig 4B, we do detect Cin8-GFP in quiescent cells.

> - *Quantification is needed in Figure 4 panels c) and h).*

Fig 4C and 4H have been changed and quantification are provided in the figure legend.

> ***Reviewer #3 (Recommendations For The Authors):***
>
> *A few points should be addressed for clarity:*
>
> *(1) Sup. Fig. 1K: are only viable cells used for the colony-forming assay? How were these selected? If not, the assay would just measure survival (as in the viability assay).*

Yes, only viable cells were selected for the colony forming assay. We used methylene blue to stain dead cells. Then, we used a micromanipulation instrument (Singer Spore Play) that is commonly used for tetrad dissection to select “non blue cells” and position them on a plate (as we do with spores). Each micromanipulated cell is then allowed to grow on the plate and we count colonies (see picture in Sup Fig 1L right panel). This was described in Laporte et al, JCB 2011. We have added that piece of information in the legend (line 1129-1130) and in the M&M section (line 580-586).

> *(2) Could Tub3 have a role in phase I? It is not clear why the authors conclude involvement only in phase II.*

As it can be seen in Fig 2D, MT bundle length and thickness are quite similar in WT and Tub1-only cells in phase I, indicating that the absence of Tub3 as no effect in phase I. In Tub1-only cells, MT bundles are thinner in both phase II and phase III, yet, they get fully stabilized in phase III. Thus, the effect of Tub3 is largely specific to the nucleation/elongation of phase II MTs. We hope to have clarified that point in the text (line 203-207).

> *(3) Quantifications, statistics: for all quantifications, the authors should clearly state the number of experiments (replicates), and number of cells used in each, and what number was used for statistics. For all quantifications in cells, it seems that the values from the total number of cells across different experiments were plotted and used for statistics. This is not very useful and results in extremely small p values. I assume that the values for individual cells were obtained from multiple, independent experiments. Unless there are technical limitations that allow only a very small sample size (not the case here for most experiments), for experiments involving treatments the authors should determine values for each experiment and show statistics for comparison between experiments rather than individual cells pooled from multiple experiments.*

All the experiments have been done at least in replicate. In the new Fig. 1A, we now display each independent experiment with a specific color code. For Fig 2B and 2C we now provide the data obtained for each separate experiment in Sup Fig 2C. Additional details about quantifications and statistics are provided in the M&M section or in the specific figure legends.